Geochemistry, Geophysics, Geosystems®

AGU ADVANCING EARTH AND SPACE SCIENCE

RESEARCH ARTICLE
10.1029/2021GC009859

**Key Points:**

- A comprehensive geothermometric investigation of the New Caledonia ophiolite has been carried out
- The computed temperatures and cooling rates (≈$10^{-4}$–$10^{-3}$°C/y) contrast with previous results on ophiolitic and forearc peridotites
- The thermal conditions recorded by forearc sequences can be linked to specific areal processes and previous lithosphere evolution

**Supporting Information:**

Supporting Information may be found in the online version of this article.

**Correspondence to:**

A. Montanini,
alessandra.montanini@unipr.it

**Citation:**

Secchiari, A., Montanini, A., & Cluzel, D. (2022). Temperatures and cooling rates recorded by the New Caledonia ophiolite: Implications for cooling mechanisms in young forearc sequences. *Geochemistry, Geophysics, Geosystems*, *23*, e2021GC009859. https://doi.org/10.1029/2021GC009859

Received 28 APR 2021
Accepted 22 DEC 2021

**Author Contributions:**

**Conceptualization:** Arianna Secchiari, Alessandra Montanini
**Data curation:** Arianna Secchiari
**Formal analysis:** Arianna Secchiari
**Investigation:** Arianna Secchiari
**Methodology:** Arianna Secchiari
**Resources:** Arianna Secchiari
**Validation:** Arianna Secchiari, Alessandra Montanini
**Writing – original draft:** Arianna Secchiari, Alessandra Montanini



# Temperatures and Cooling Rates Recorded by the New Caledonia Ophiolite: Implications for Cooling Mechanisms in Young Forearc Sequences

**Arianna Secchiari[1], Alessandra Montanini[1], and Dominique Cluzel[2]**

[1]Department of Chemistry, Life Sciences and Environmental Sustainability, University of Parma, Parma, Italy, [2]Institut des Sciences Exactes et Appliquées, Université de la Nouvelle-Calédonie, Noumea, New Caledonia

**Abstract** To unveil how forearc lithosphere cools and re-equilibrates, we carried out a comprehensive geothermometric investigation of the New Caledonia ophiolite, which represents a rare example of proto-arc section generated during subduction infancy. A large data set, including more than 80 samples (peridotites and mafic-ultramafic intrusives), was considered. Closure temperatures calculated for the lherzolites using slow ($T_{REE\text{-}Y}$) and fast diffusing ($T_{Ca\text{-}in\text{-}Opx}$, $T_{BKN}$, $T_{Ca\text{-}in\text{-}Ol}$, $T_{Ol\text{-}Sp}$) geothermometers provide some of the highest values ever documented for ophiolitic peridotites, akin to modern sub-oceanic mantle. Cooling rates deduced from $T_{REE\text{-}Y}$ and $T_{BKN}$ yield values of ≈$10^{-3}$°C/y, similar to those obtained with $T_{Ca\text{-}in\text{-}Ol}$. These features are consistent with a post-melting history of emplacement, possibly along a transform fault, and thermal re-equilibration via conduction. Cpx-free harzburgites register a high-T evolution, followed by quenching and obduction. The relatively high $T_{Ca\text{-}in\text{-}Ol}$, $T_{Ol\text{-}Sp}$ and cooling rates computed from $T_{Ca\text{-}in\text{-}Ol}$ (≈$10^{-3}$°C/y) are atypical for this geodynamic setting, mirroring the development of an ephemeral subduction system, uplift and emplacement of the Peridotite Nappe. Temperature profiles across the crust-mantle transect point to high closure temperatures, with limited variations with depth. These results are indicative of injection and crystallization of non-cogenetic magma batches in the forearc lithosphere, followed by thermal re-equilibration at rates of ≈$10^{-4}$–$10^{-3}$°C/y. Our study shows that the thermal conditions recorded by forearc sequences are intimately related to specific areal processes and previous lithospheric evolution. Thus, detailed sampling and exhaustive knowledge of the geological background are critical to unravel the cooling mechanisms in this geodynamic setting.

**Plain Language Summary** The New Caledonia ophiolite represents a rare example of a complete forearc section, extending from the lower crust to the mantle, originated at the beginning of the Eocene subduction. Our study aims to shed light on the thermal evolution of this ophiolite, which constitutes one of the largest ophiolite complexes worldwide, gaining-at the same time - insights into the mechanisms that govern cooling of forearc lithosphere. For this purpose, different geothermometers were applied to mantle peridotite and mafic-ultramafic intrusive samples. Geothermometers are equations based on temperature-dependent major element and/or trace element exchange reactions among mineral phases, which allow calculating equilibrium temperatures starting from mineral chemical compositions. Equilibrium temperatures obtained with various thermometers can be linked to the cooling evolution and heat extraction rates of the studied samples. With this study, we were able to track the post-melting evolution and re-equilibration at lower temperature conditions for all the investigated rock types. A comprehensive investigation of the Massif du Sud sequence, from the lower crust to the upper mantle, allowed us to build thermal profiles across the forearc lithosphere. Overall, our results contribute to unravel the cooling mechanisms of the crust-mantle sequences in this poorly explored tectonic setting.

## 1. Introduction

Chemical geothermometers are powerful tools to unravel the thermal history of mafic and ultramafic lithologies. They allow to calculate closure temperatures starting from measured mineral compositions using temperature-dependent major elements (e.g., Brey & Köhler, 1990; Putirka, 2008; Wells, 1977) and/or trace element exchange reactions among mineral phases (e.g., Lee et al., 2007; Liang et al., 2013; Sun & Liang, 2014).

Results obtained from major and trace element thermometry strongly depend on the thermal evolution and cooling rates experienced by the analyzed samples. Chemical geothermometers applied to rock samples thermally equilibrated over long geological times, which undergo rapid exhumation and/or eruption, are expected to yield

**Writing – review & editing:** Arianna Secchiari, Alessandra Montanini, Dominique Cluzel

homogeneous temperatures, corresponding to their equilibration conditions. Hence, no information related to their thermal evolution will be available for such samples. This is the case of mantle xenoliths from continental lithosphere brought to the surface by intraplate volcanism (e.g., Liang et al., 2013 and references therein; Guo et al., 2019).

By contrast, for samples that cooled relatively slowly to allow appreciable diffusive re-equilibration to occur among mineral phases during cooling, the application of different chemical thermometers will provide a range of temperatures. More specifically, geothermometers will show higher temperatures for samples with faster cooling rates. In this case, geothermometers will be able to track the thermal evolution of the studied lithologies.

Temperatures calculated with a given thermometer are related to the intercrystalline diffusion rates of the elements (or components) used to calibrate the thermometer. In detail, slowly diffusing element-based thermometers can preserve the highest closure temperatures (e.g., the REE + Y Cpx-Opx thermometer: Liang et al., 2013), while fast diffusing element-based thermometers will indicate low equilibration temperatures (Dygert & Liang, 2015; Hanghøj et al., 2010; Liang et al., 2013).

Although the combined application of different thermometers represents a powerful tool to shed light on the thermal regimes experienced by the ophiolitic complexes during their lifetime, only a few studies have been performed. These works mostly focused on ophiolites with little or no subduction influence, or formed at fossil Mid Ocean Ridges (e.g., Dygert & Liang, 2015; Dygert et al., 2017; Smye et al., 2017), while ophiolites showing strong subduction influence remain a relatively unexplored field of investigation. Thus, our current knowledge of the cooling mechanisms of subduction-related mantle sequences is scarce.

To bridge this gap of knowledge, we have carried out a detailed geothermometric investigation of the New Caledonia ophiolite. This ophiolite constitutes one of the rare examples of a complete forearc sequence originated during subduction inception (Cluzel, Maurizot et al., 2012), thus providing the opportunity to investigate cooling mechanisms in a young forearc section. To unravel the thermal history of the ophiolite, we have applied different chemical thermometers to well-characterized mantle peridotites (lherzolites and harzburgites) from different massifs and to mafic-ultramafic samples (gabbronorites, wehrlites, pyroxenites, and dunites) belonging to the so-called "cumulitic sequence" of the Massif du Sud. To give a full and representative picture of the thermal evolution of the ophiolite, we have based our study on a robust data set, including more than 80 samples. Most of the data are compiled from previous geochemical and petrological studies (i.e., Marchesi et al., 2009; Pirard et al., 2013; Secchiari et al., 2016, 2018, 2020; Xu et al., 2020) but new unpublished data were also included.

With this study, we aim to: (a) unravel, for the first time, the cooling history and the thermal evolution of an infant proto-arc section; (b) draw new insights into the thermal regime experienced by one of the biggest ophiolitic complexes worldwide; (c) compare our results with data on modern analogs and other ophiolitic sequences worldwide.

## 2. Geological and Petrological Background

The New Caledonia archipelago lies in the SW Pacific Ocean, between the New Hebrides Arc and the eastern margin of Australia (Figure 1). The main island of New Caledonia (i.e., Grande Terre) constitutes ~90% of the land area and is composed of an assemblage of volcanic, sedimentary, and metamorphic terranes, ranging in age from Permian to Miocene (e.g., Aitchison et al., 1995; Cluzel, Maurizot et al., 2012, 2001; Lagabrielle et al., 2013). Pre-Late Cretaceous tectonic events led to the accretion of these terranes onto the eastern Australian margin of Gondwanaland (e.g., Aitchison et al., 1995; Cluzel, Maurizot et al., 2012; Schellart et al., 2006; Whattam, 2009).

Starting from Late Cretaceous, the tectonic evolution of the Southwest Pacific Region included marginal basins opening (i.e., Tasman Sea, New Caledonia, Loyalty/South Loyalty basins) that isolated continental strips of Paleozoic-Jurassic age and renewed island arc formation.

The present-day structure of New Caledonia mostly resulted from a Paleogene episode of convergence related to the closure of the South Loyalty basin, which initiated at ~56 Ma, (Cluzel, Maurizot et al., 2012) and gave birth to

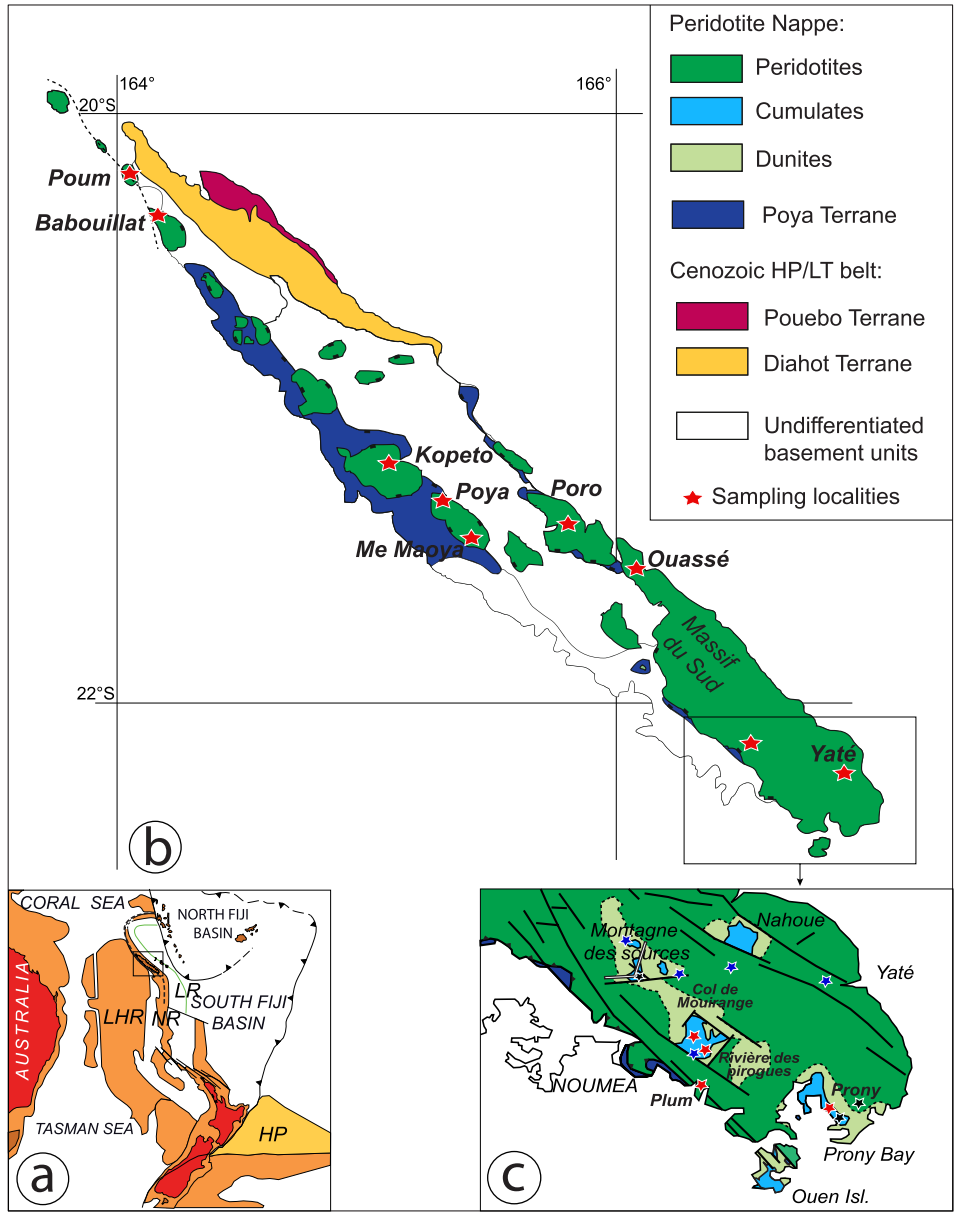


**Figure 1.** (a) Present-day structures of the Southwest Pacific region. Red, land; light orange, continental plateau; white, oceanic basins (LHR: Lord Howe Rise, NR: Norfolk ridge, LR: Loyalty ridge, HP: Hikurangi Plateau); (b) simplified geological map of New Caledonia showing the distribution of the Peridotite massifs and sampling locations; (c) simplified sketch map of the southern part of the Massif du Sud. Red stars: sampling areas for the gabbronorites (Secchiari et al., 2018, see Table 1). Black and blue stars are sampling locations of the mafic-ultramafic sequence and the harzburgites from the work of Marchesi et al. (2009) and Pirard et al. (2013), respectively. Modified after Cluzel, Maurizot et al. (2012) and Secchiari et al. (2018).

supra-subduction dykes during the 55–50 Ma interval (Cluzel et al., 2006). Microcontinent-arc collision resulted in the failure of an Eocene NE-dipping subduction (Aitchison et al., 1995; Cluzel et al., 2001, Cluzel, Maurizot et al., 2012, 2020), culminating in the obduction of the ophiolitic units at ~34 Ma (Cluzel, Jourdan et al., 2012).

The samples of this study belong to the "Peridotite Nappe" (Avias, 1967), a large sheet of obducted mantle rocks rooted in the Loyalty basin. Apart from some sparse tectonic klippen, the Peridotite Nappe is mostly exposed in the Massif du Sud, where a ~2,500 m thick harzburgite-dunite sequence, locally overlain by km-scale lenses of mafic and ultramafic intrusions, crops out. This sequence represents one of the few exposed crust-mantle

transects worldwide, generated at the onset of subduction in a nascent arc setting (Marchesi et al., 2009; Pirard et al., 2013; Secchiari et al., 2018). Recent geochemical studies have shown that the dunites and wehrlites have a replacive origin and originated by interaction between a residual mantle sequence and boninitic and arc-tholeiitic magmas (Marchesi et al., 2009; Pirard et al., 2013). Up section, the progressive appearance of orthopyroxene and plagioclase marks the transition to layered dunites, wehrlites/pyroxenites, and, finally, gabbronorites. The layered textures recognized in most gabbronorite outcrops have been ascribed to a cumulitic origin (Marchesi et al., 2009; Pirard et al., 2013; Secchiari et al., 2018). Derivation from magma batches transitional between boninites and tholeiites with a highly depleted trace element signature has been speculated for the gabbronorites (Marchesi et al., 2009; Pirard et al., 2013; Secchiari et al., 2018).

Harzburgites are the dominant lithotype of the Peridotite Nappe. They bear an overall refractory composition, testified by exceedingly low contents of incompatible trace elements and the remarkable absence of primary clinopyroxene (Marchesi et al., 2009; Prinzhofer & Allègre, 1985; Secchiari et al., 2019, 2020; Ulrich et al., 2010). Geochemical studies proposed that the harzburgites acquired their signature through high degrees of fluid-assisted melting above the Eocene subduction zone (~20%-25%, see Marchesi et al., 2009; Ulrich et al., 2010). More recently, Secchiari et al. (2020) proposed that whole rock and orthopyroxene trace element compositions of the harzburgites are consistent with two partial melting episodes in the spinel stability field. A first (undated) melting event likely occurred in a MOR setting and was followed by further melting in a supra-subduction zone environment during the Eocene (Secchiari et al., 2019, 2020) and post-melting metasomatism, resulting in secondary ortho- and clinopyroxene precipitation (Figure S1 in Supporting Information S1).

Minor spinel and plagioclase-bearing lherzolites (Figure S1 in Supporting Information S1) occur in the northernmost part of the island (Secchiari et al., 2016; Ulrich et al., 2010). Unlike the central and southern harzburgitic massifs, the lherzolites do not record a strong subduction fingerprint. Trace element geochemical modeling indicates that their signature could be reproduced by a moderate degree of melt extraction of a depleted mantle source (~8%–9%), started in the garnet stability field. By contrast, plagioclase lherzolites originated from residual spinel lherzolites through reactive percolation and entrapment of depleted MORB melts in the shallow oceanic lithosphere (Secchiari et al., 2016). As a whole, the petrological and geochemical features displayed by the New Caledonia lherzolites reflect an origin in a spreading ridge environment, possibly a marginal basin predating the Eocene subduction (Secchiari et al., 2016). To date, the relationships between the northern lherzolites and the ultra-depleted harzburgites are difficult to ascertain, based on the available petrological and geochemical data (Secchiari et al., 2020; Ulrich et al., 2010).

## 3. Methods and Data Sources

To reconstruct the thermal evolution of the New Caledonia ophiolite, geothermometric calculations for a set of 87 samples have been carried out. We report thermometric data for 58 peridotites and 29 mafic and ultramafic intrusives (see Tables 1 and 2). Sampled lithologies include: (a) spinel and plagioclase lherzolites from the northern massifs; (b) depleted harzburgites from central and western tectonic klippen and Massif du Sud; (c) mafic and ultramafic rocks from the Massif du Sud, namely cumulitic gabbros, wehrlites, pyroxenites and dunites. The modal compositions of the investigated rock types are reported in Table S1.

To calculate equilibrium temperatures, pyroxene, olivine, plagioclase, and spinel major element compositions were taken from the literature (Secchiari et al., 2016, 2018, 2020; Marchesi et al., 2009; Pirard et al., 2013; Xu et al., 2020). Moreover, to expand the available data, six unpublished analyses (Tables 1 and 2) were added to our data set. For pyroxene and plagioclase trace element contents, we used data from Secchiari et al. (2016, 2018).

All the data sources analyzed in situ major element composition using a microprobe or a scanning electron microscope (see Table S2 and references for further detail), while pyroxene and plagioclase trace element data (Secchiari et al., 2016, 2018) were measured using laser ablation inductively coupled mass spectrometry (LA-ICP-MS, Table S2).

Major element mineral data for the studied samples are reported in Table S3 and Figure S2 in Supporting Information S1. Trace element contents of the analyzed minerals and chondrite-normalized REE patterns are re-

**Table 1**
*Equilibrium Temperatures and Cooling Rates Calculated for the New Caledonia Peridotites*

| Sample | Locality | Lithology | Source | $T_{REE-Y}$ | ±1σ | $T_{BKN}$ | $T_{Ta}$ | $T_{Ca\text{-}in\text{-}Opx}$ | $T_{Ca\text{-}in\text{-}Ol}$ | $T_{Ol\text{-}Sp}$ | Opx radius (mm)[b] | dT/dt (°C/y) from $T_{REE-Y}$ and $T_{BKN}$ | Ol radius (mm)[b] | dT/dt (°C/y) from $T_{Ca\text{-}in\text{-}Ol}$ |
|---|---|---|---|---|---|---|---|---|---|---|---|---|---|---|
| BA1 | Babouillat | Spl lherzolite | Secchiari et al. (2016) | 1334 | 39 | 955 | 960 | 1031 | 824 | 863 | 2.5 | 4.00E−03 | 1.0 | 1.17E−03 |
| BAB1B | Babouillat | Pl lherzolite | Secchiari et al. (2016) | 1314 | 24 | 993 | 1026 | 1082 | 828 | 888 | 2.5 | 4.00E−03 | 1.0 | 1.27E−03 |
| BAB2A | Babouillat | Pl lherzolite | Secchiari et al. (2016) | 1381 | 7 | 847 | 844 | 1074 | 865 | 794 | – | – | 1.0 | 2.85E−03 |
| BAB2B | Babouillat | Pl lherzolite | Secchiari et al. (2016) | 1394 | 25 | 776 | 758 | 1027 | 873 | 906 | – | – | 1.0 | 3.34E−03 |
| POU2 | Poum | Spl lherzolite | Secchiari et al. (2016) | 1256 | 11 | 946 | 967 | 1055 | 893 | 950 | 2.5 | 4.00E−03 | 1.0 | 5.10E−03 |
| POU1A | Poum | Pl lherzolite | Secchiari et al. (2016) | 1311 | 33 | 861 | 876 | 1010 | 847 | 910 | – | – | 1.0 | 1.93E−03 |
| KPT1[a] | Kopeto | Harzburgite | Secchiari et al. (2020) | – | – | – | – | 1125 | 853 | 965 | – | – | 0.8 | 3.43E−03 |
| KPT3[a] | Kopeto | Harzburgite | Secchiari et al. (2020) | – | – | – | – | 1024 | 769 | 890 | – | – | 0.8 | 4.99E−04 |
| KPT5[a] | Kopeto | Spl harzburgite | Secchiari et al. (2020) | – | – | – | – | 1030 | 766 | 840 | – | – | 0.8 | 4.58E−04 |
| PY1[a] | Poya | Spl harzburgite | Secchiari et al. (2020) | – | – | e | – | 1017 | – | 930 | – | – | – | – |
| PO3[a] | Poro | Spl harzburgite | Secchiari et al. (2020) | – | – | – | – | 986 | – | 940 | – | – | – | – |
| PO4[a] | Poro | Spl harzburgite | Secchiari et al. (2020) | – | – | – | – | – | 811 | – | – | – | 0.8 | 1.35E−03 |
| YA1[a] | Yaté | Spl harzburgite | Secchiari et al. (2020) | – | – | – | – | 1020 | 810 | 815 | – | – | 1.0 | 8.44E−04 |
| MM1[a] | Me Maoya | Spl harzburgite | Secchiari et al., this work | – | – | – | – | 976 | – | 910 | – | – | – | – |
| MM2[a] | Me Maoya | Spl harzburgite | Secchiari et al., this work | – | – | – | – | 1011 | – | 900 | – | – | – | – |
| TT4A[a] | Tontouta valley | Harzburgite | Marchesi et al. (2009) | – | – | – | – | 991 | 884 | 933 | – | – | 1.0 | 4.26E−03 |
| TT14[a] | Tontouta valley | Harzburgite | Marchesi et al. (2009) | – | – | – | – | 1095 | 851 | 954 | – | – | 1.0 | 2.14E−03 |
| TT17[a] | Tontouta valley | Harzburgite | Marchesi et al. (2009) | – | – | – | – | 1070 | 851 | – | – | – | 1.0 | 2.14E−03 |
| PR 4B[a] | Prony | Harzburgite | Marchesi et al. (2009) | – | – | – | – | 1008 | 808 | – | – | – | 1.0 | 8.12E−04 |
| PR 5B[a] | Prony | Harzburgite | Marchesi et al. (2009) | – | – | – | – | 986 | 851 | – | – | – | 1.0 | 2.12E−03 |
| YA5[a] | Yaté | Harzburgite | Pirard et al. (2013) | – | – | – | – | 929 | 892 | – | – | – | 1.0 | 4.98E−03 |
| PRB58b[a] | Parc de la Rivière Bleue | Harzburgite | Pirard et al. (2013) | – | – | – | – | 1106 | 938 | 931 | – | – | 1.0 | 1.20E−02 |
| PRB61f[a] | Parc de la Rivière Bleue | Harzburgite | Pirard et al. (2013) | – | – | – | – | – | 894 | 875 | – | – | 1.0 | 5.18E−03 |

**Table 1**
*Continued*

| Sample | Locality | Lithology | Source | $T_{REE-Y}$ | ±1σ | $T_{BKN}$ | $T_{Ta}$ | $T_{Ca-in-Opx}$ | $T_{Ca-in-Ol}$ | $T_{Ol-Sp}$ | Opx radius (mm)[b] | dT/dt (°C/y) from $T_{REE-Y}$ and $T_{BKN}$ | Ol radius (mm)[b] | dT/dt (°C/y) from $T_{Ca-in-Ol}$ |
|---|---|---|---|---|---|---|---|---|---|---|---|---|---|---|
| PRB75[a] | Parc de la Rivière Bleue | Harzburgite | Pirard et al. (2013) | – | – | – | – | 972 | 902 | 910 | – | – | 1.0 | 6.10E−03 |
| 15NC01[a] | Ouassé Bay | Harzburgite | Xu et al. (2020) | – | – | – | – | 1067 | 851 | 907 | – | – | 1.0 | 2.14E−03 |
| 15NC02[a] | Ouassé Bay | Harzburgite | Xu et al. (2020) | – | – | – | – | 916 | 808 | 858 | – | – | 1.0 | 8.12E−04 |
| 15NC03[a] | Ouassé Bay | Harzburgite | Xu et al. (2020) | – | – | – | – | 1116 | 851 | 974 | – | – | 1.0 | 2.14E−03 |
| 15NC04[a] | Ouassé Bay | Harzburgite | Xu et al. (2020) | – | – | – | – | 1145 | 808 | 844 | – | – | 1.0 | 8.12E−04 |
| 15NC05[a] | Ouassé Bay | Harzburgite | Xu et al. (2020) | – | – | – | – | 1000 | 851 | 942 | – | – | 1.0 | 2.14E−03 |
| 15NC06[a] | Ouassé Bay | Harzburgite | Xu et al. (2020) | – | – | – | – | 903 | 851 | 981 | – | – | 1.0 | 2.14E−03 |
| 15NC07[a] | Ouassé Bay | Harzburgite | Xu et al. (2020) | – | – | – | – | 1037 | 808 | 950 | – | – | 1.0 | 8.12E−04 |
| 15NC08[a] | Ouassé Bay | Harzburgite | Xu et al. (2020) | – | – | – | – | 1089 | 884 | 953 | – | – | 1.0 | 4.26E−03 |
| 15NC09[a] | Ouassé Bay | Harzburgite | Xu et al. (2020) | – | – | – | – | 923 | 851 | 954 | – | – | 1.0 | 2.14E−03 |
| 15NC11[a] | Me Maoya | Harzburgite | Xu et al. (2020) | – | – | – | – | 996 | 851 | 887 | – | – | 1.0 | 2.14E−03 |
| 15NC12[a] | Me Maoya | Harzburgite | Xu et al. (2020) | – | – | – | – | 1100 | 808 | 888 | – | – | 1.0 | 8.12E−04 |
| 15NC13[a] | Me Maoya | Harzburgite | Xu et al. (2020) | – | – | – | – | 985 | 851 | 980 | – | – | 1.0 | 2.14E−03 |
| 15NC15[a] | Me Maoya | Harzburgite | Xu et al. (2020) | – | – | – | – | 1003 | 851 | 949 | – | – | 1.0 | 2.14E−03 |
| 15NC17[a] | Me Maoya | Harzburgite | Xu et al. (2020) | – | – | – | – | 1039 | 884 | 912 | – | – | 1.0 | 4.26E−03 |
| 15NC20[a] | Me Maoya | Harzburgite | Xu et al. (2020) | – | – | – | – | 1116 | 851 | 928 | – | – | 1.0 | 2.14E−03 |
| 15NC21[a] | Me Maoya | Harzburgite | Xu et al. (2020) | – | – | – | – | 1025 | 808 | 931 | – | – | 1.0 | 8.12E−04 |
| 15NC22[a] | Me Maoya | Harzburgite | Xu et al. (2020) | – | – | – | – | 1065 | 884 | 943 | – | – | 1.0 | 4.26E−03 |
| 15NC23[a] | Me Maoya | Harzburgite | Xu et al. (2020) | – | – | – | – | 935 | 808 | 933 | – | – | 1.0 | 8.12E−04 |
| 15NC24[a] | Me Maoya | Harzburgite | Xu et al. (2020) | – | – | – | – | 1006 | 851 | 945 | – | – | 1.0 | 2.14E−03 |
| 15NC25[a] | Me Maoya | Harzburgite | Xu et al. (2020) | – | – | – | – | 1030 | 808 | 942 | – | – | 1.0 | 8.12E−04 |
| 15NC26[a] | Me Maoya | Harzburgite | Xu et al. (2020) | – | – | – | – | 1102 | 911 | 896 | – | – | 1.0 | 7.29E−03 |
| 15NC27[a] | Me Maoya | Harzburgite | Xu et al. (2020) | – | – | – | – | 917 | 741 | 904 | – | – | 1.0 | 1.56E−04 |
| 15NC28[a] | Me Maoya | Harzburgite | Xu et al. (2020) | – | – | – | – | 1120 | 884 | 975 | – | – | 1.0 | 4.26E−03 |
| 15NC29[a] | Me Maoya | Harzburgite | Xu et al. (2020) | – | – | – | – | 977 | 851 | 906 | – | – | 1.0 | 2.14E−03 |
| 15NC30[a] | Me Maoya | Harzburgite | Xu et al. (2020) | – | – | – | – | 942 | 884 | 894 | – | – | 1.0 | 4.26E−03 |
| 15NC31[a] | Massif du Sud | Harzburgite | Xu et al. (2020) | – | – | – | – | 992 | 851 | 863 | – | – | 1.0 | 2.14E−03 |
| 15NC32[a] | Massif du Sud | Harzburgite | Xu et al. (2020) | – | – | – | – | 1028 | 808 | 901 | – | – | 1.0 | 8.12E−04 |
| 15NC33[a] | Massif du Sud | Harzburgite | Xu et al. (2020) | – | – | – | – | 1075 | 851 | 928 | – | – | 1.0 | 2.14E−03 |
| 15NC34[a] | Massif du Sud | Harzburgite | Xu et al. (2020) | – | – | – | – | 1185 | 741 | 939 | – | – | 1.0 | 1.56E−04 |
| 15NC84[a] | Massif du Sud | Harzburgite | Xu et al. (2020) | – | – | – | – | 981 | 741 | 971 | – | – | 1.0 | 1.56E−04 |
| 15NC85[a] | Massif du Sud | Harzburgite | Xu et al. (2020) | – | – | – | – | 941 | 911 | 1007 | – | – | 1.0 | 7.29E−03 |
| 15NC86[a] | Massif du Sud | Harzburgite | Xu et al. (2020) | – | – | – | – | 978 | 808 | 963 | – | – | 1.0 | 8.12E−04 |
| 15NC87[a] | Massif du Sud | Harzburgite | Xu et al. (2020) | – | – | – | – | 954 | 851 | 970 | – | – | 1.0 | 2.14E−03 |
| 15NC88[a] | Massif du Sud | Harzburgite | Xu et al. (2020) | – | – | – | – | 955 | 851 | 910 | – | – | 1.0 | 2.14E−03 |

*Note*. $T_{REE-Y}$ = REE-Y-in-two-pyroxene thermometer (Liang et al., 2013); $T_{BKN}$-$T_{Ta}$ = two-pyroxene solvus thermometers (Brey & Köhler, 1990; Taylor, 1998); $T_{Ca-in-Opx}$ = Ca in orthopyroxene thermometer (Brey & Köhler, 1990); $T_{Ca-in-Ol}$ = Ca in olivine thermometer (De Hoog et al., 2010); $T_{Ol-Sp}$ = olivine-spinel Fe-Mg thermometer (Li et al., 1995). σ: standard deviation of calculated $T_{REE-Y}$. Temperatures were computed using average compositions of porphyroclastic cores and assuming a pressure of 10 kbar.

[a]Cpx-free harzburgites: for these samples $T_{Ca-in-Opx}$ represent minimum temperature estimates under the assumption that orthopyroxene composition reflects equilibrium with clinopyroxene. [b]Olivine grain radius = average olivine grain radius used for calculations of cooling rates based on $T_{Ca-in-Ol}$. Olivine grain radius was deduced from petrographic observations for samples from Secchiari et al. (2016, 2020). For other literature data (Marchesi et al., 2009; Pirard et al., 2013; Xu et al., 2020) an average olivine grain radius of 1 mm was assumed. See text for further details.

ported in Table S4 and Figure 2. The mineral phases used in this study display remarkably homogeneous major and trace element compositions, as revealed from the detailed analytical work carried out on these lithologies (see references and Table S2). Significant chemical zoning, for both major and trace elements, is lacking in the mineral phases at the grain size, and intrasample variability appear notably limited (Table S3). Owing to the compositional homogeneity and the excellent analytical quality of the literature data, we believe that the results presented in this work may be representative of the thermal state of the ophiolite. For computing closure temperatures for the various lithologies, average mineral compositions from grain cores were used, in order to avoid possible grain boundaries disturbance. We applied different types of geothermometers: (a) REE-in-two-pyroxene thermometer of Liang et al. (2013), which is based on the composition-dependent temperature sensitivity of REEs + Y exchange between ortho- and clinopyroxene; (b) REE-in-plagioclase-clinopyroxene thermometer (Sun & Liang, 2017), which uses REEs + Y partitioning between coexisting plagioclase and clinopyroxene; (c) two-pyroxene solvus thermometers (Brey & Köhler, 1990; Taylor, 1998), which parameterize temperature-sensitive transfer of the enstatite component between coexisting ortho- and clinopyroxene around the miscibility gap; (d) cation exchange thermometers, based on the temperature sensitivity of intercrystalline exchange of major and trace elements: Ca-in-orthopyroxene, olivine-spinel and Ca-in-olivine thermometers (Brey & Köhler, 1990; De Hoog et al., 2010; Li et al., 1995). In addition, melting temperatures or mantle peridotites were obtained for the lherzolites using the formulation of Lee and Chin (2014).

Due to the absence of primary clinopyroxene in the harzburgites, two-pyroxene geothermometers have been applied only to the lherzolites and to some mafic-ultramafic clinopyroxene-bearing intrusives, where the two pyroxenes appeared to be in textural equilibrium. Thus, owing to the depleted nature of the harzburgites, the application of chemical geothermometers is limited to orthopyroxene, olivine, and olivine-spinel based thermometers.

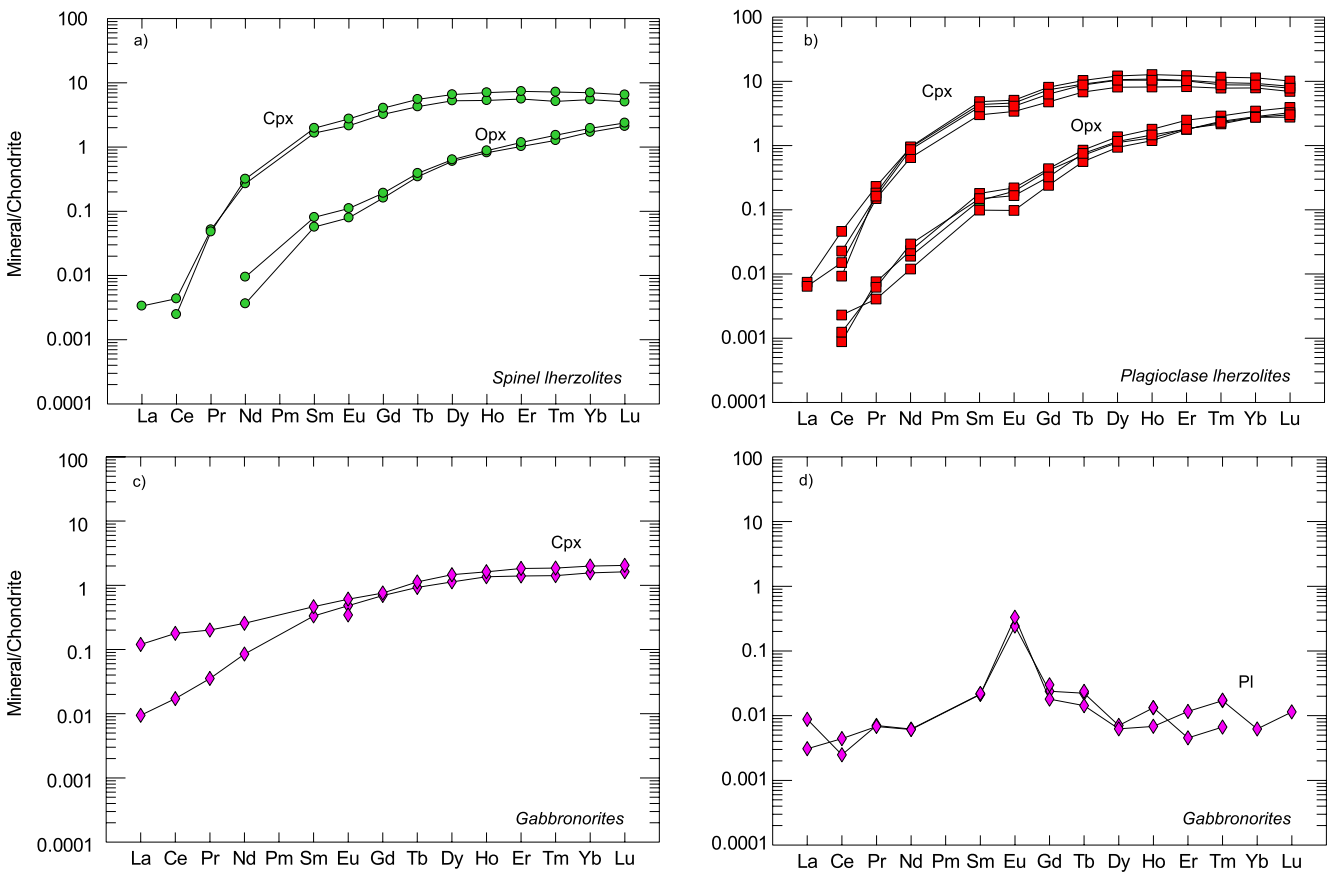


**Figure 2.** Chondrite-normalized REE compositions of (a) clino- and orthopyroxene from the New Caledonia spinel lherzolites and (b) plagioclase lherzolites (Secchiari et al., 2016); (c) clinopyroxene and (d) plagioclase from the New Caledonia gabbronorites (Secchiari et al., 2018). Plotted values represent average values for each sample. Error bars are smaller or equal to the symbol size.

## 4. Results

### 4.1. REE + Y Compositions of Ortho- and Clinopyroxenes Used for T Calculations

Clino- and orthopyroxene from spinel lherzolites have subparallel REE patterns (Figures 2a and 2b), similar to abyssal-type peridotites (e.g., Johnson et al., 1990; Warren et al., 2009). Slightly higher REE contents are recorded by plagioclase-bearing rocks (Figure 2b). Clinopyroxene displays depleted LREE, relatively flat HREE ($Tb_N/Yb_N = 0.79–1.0$) and MREE/HREE fractionation ($Sm_N/Yb_N = 0.28–0.47$). For some samples, a slight enrichment in La and Ce can be observed. Orthopyroxene from both spinel and plagioclase lherzolites exhibits very depleted compositions, with distinctly lower REE concentrations compared to clinopyroxene, and steeply plunging patterns ($Gd_N/Yb_N$ = 0.09–0.15). Small negative Eu anomalies (Eu/Eu* = 0.57–0.84) were detected for both clino-and orthopyroxene in plagioclase-bearing lherzolites, due to equilibration with plagioclase.

REE concentrations in clinopyroxene from gabbronorites are strikingly low, with HREE varying between 0.8–2 times chondritic values (Figure 2c). Clinopyroxene REE patterns are characterized by gently sloping profiles, with a progressive increase in concentrations from LREE to HREE ($Ce_N/Yb_N$ = 0.01–0.09) and weakly concave-downward patterns for $Yb_N$ = 0.93–1.72. The highly calcic plagioclase (Table S3) also exhibits depleted trace element composition, characterized by flat to slightly enriched LREE, between 0.003 and 0.13 times chondrite, and prominent Eu positive anomaly (Eu/Eu* = 11–18, see Figure 2d).

### 4.2. Temperature Inversion

As the analyzed minerals do not display significant core-rim compositional variations or intra-sample variability, temperatures were computed using representative average mineral compositions from pyroxene grain cores and cores of clinopyroxene-plagioclase pairs, which generally exhibit low standard deviation values (Table 1, Figure 2). Temperatures were then inverted from the trace element data using the methods discussed in the works of Liang et al. (2013) and Sun and Liang (2017) for the lherzolites and the gabbronorites, respectively.

To assess data quality and consistency for REE-in-two-pyroxene and REE-in-plagioclase-clinopyroxene thermometers, REE abundances were first plotted on chondrite normalized diagrams (Figure 2). Particular attention was devoted to LREE enrichments, which could be a hint of metasomatic processes, and to the smoothness of the REE patterns. Equilibrium conditions between two pyroxenes and plagioclase-clinopyroxene pairs were also evaluated plotting the ratios of the measured REE + Y concentrations in pyroxenes and plagioclase against their ionic radii (Figure 3).

REEs-Y data were then plotted for each sample in the inversion diagram, that is, ln (D–A) versus B, where D represents the partition coefficient between ortho- and clinopyroxene or plagioclase and clinopyroxene for REE-in-two-pyroxene and REE-in-plagioclase-clinopyroxene thermometers, and A and B are coefficients determined by major-element compositions and REE ionic radius, respectively (Liang et al., 2013). A line anchored at the origin was then drawn, by fitting the measured data using robust regression method (see Figure S3 in Supporting Information S1). The slope of the line is ideally the temperature, and it should overlie all the measured data. In case of scatter from the fitting line, outliers were manually excluded in the reversion analysis and a meaningful temperature was obtained from the linear data. Each sample was carefully examined before being added to or omitted from a database of approved temperatures. Figures generated for the main text of this study only include approved data, which are reported in Tables 1 and 2.

### 4.3. Pressure Estimates

Owing to the lack of geobarometers in garnet- or plagioclase-free systems, a pressure equal to 10 kbar was assumed for mantle rocks for temperature calculation. A pressure estimate of 10 kbar is reasonable for samples from both mid-ocean ridge and subduction zones and allows comparison with other literature data.

For the mafic-ultramafic sequence, the depth of crystallization was calculated using the FACE geobarometer (Fumagalli et al., 2017), which relies on the pressure-sensitive equilibrium Forsterite + Anorthite = Ca-Tschermak + Enstatite. The pressure estimates were obtained for five plagioclase-bearing samples, that is, three gabbronorites and two wehrlites (see Table 2), yielding $P$ = 1.9–2.8 kbar and 3.0–3.2 kbar, respectively. Application

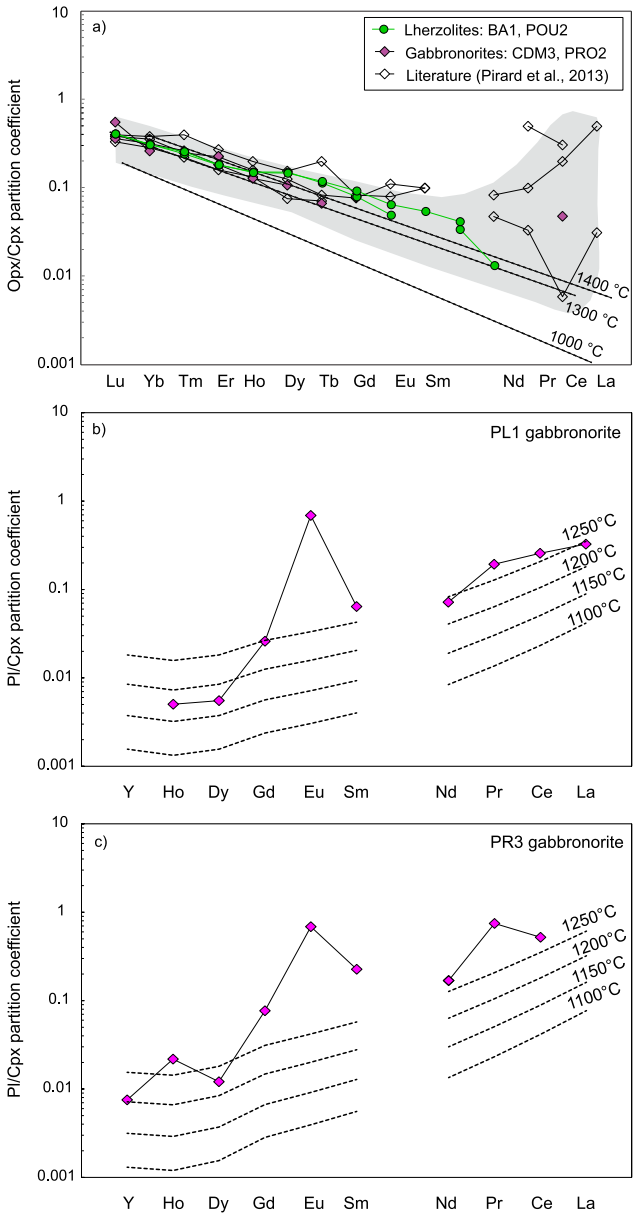


**Figure 3.** (a) Orthopyroxene/clinopyroxene REE partition coefficients calculated for the New Caledonia lherzolites and gabbronorites. The lherzolites follow the opx/cpx partitioning trends predicted for temperatures of 1300–1400°C, while the gabbronorites depict scattered trends, indicative of pyroxenes disequilibrium. Opx/cpx partitioning trends at 1000°C, 1300°C and 1400°C are from Lee et al. (2007). Grey area = abyssal peridotites field. (b–c) Plagioclase/clinopyroxene REE-Y ratios plotted against their ionic radius for PL1 and PR3 gabbronorites, respectively. Equilibration temperature lines were calculated based on mineral major element compositions compositions using the Plagioclase/clinopyroxene partitioning model of Sun and Liang (2014) and Sun and Liang (2017).

of the Fumagalli et al. (2017) geobarometer to these lithologies is expected to provide reliable estimates, as their clinopyroxene $X_{Cr}$ and $a_{CaTs}$ are similar to those of the peridotite samples used to calibrate the geobarometer (e.g., Basch et al., 2019). When the FACE geobarometer could not be applied, a pressure of 2 kbar was chosen for the gabbronorites, while a slightly higher pressure (i.e., 3 kbar) was assumed for the wehrlites and the dunites of the cumulitic sequence.

### 4.4. T Estimates

The results of T calculations are summarized in Tables 1–3

REE-in-two-pyroxene geothermometer ($T_{REE-Y}$, i.e., Liang et al., 2013) for the spinel lherzolites provide temperatures ranging between 1256–1334°C (Table 1), with the highest $T_{REE-Y}$ recorded by plagioclase lherzolites (1314–1394°C).

$T_{REE-Y}$ are not available for the mafic-ultramafic intrusives, as petrographic observations (e.g., Secchiari et al., 2018) and inversion diagrams (i.e., ln (D–A) versus B, Liang et al., 2013; Dygert & Liang, 2015) indicate disequilibrium between the two pyroxenes. The disequilibrium state is also attested by the calculated opx/cpx partition coefficients, which significantly deviate from modeling trends (e.g., Lee et al., 2007, see Figure 3). For the gabbronorites, we have applied REE-in-plagioclase-clinopyroxene thermometer ($T_{Pl-Cpx}$, i.e., Sun & Liang, 2017) after assessing plagioclase-clinopyroxene equilibrium. High-temperature values (1241–1243°C) were obtained for two samples (PL1, PR3). Despite the REE-Y pattern of PR3 gabbronorite appears a bit disturbed in Figure 3, we decided to keep $T_{Pl-Cpx}$ for this sample, as temperature inversion diagrams attest plagioclase-clinopyroxene equilibrium (Figure S3 in Supporting Information S1). Likewise, the calculated $T_{Pl-Cpx}$ is remarkably similar to PL1 gabbronorite, suggesting that the REE-Y pattern in Figure 3 may rather reflect the low trace element concentrations.

For the lherzolites, the exchange of Ca-Mg between pyroxenes ($T_{BKN}$, i.e., Brey & Köhler, 1990; $T_{Ta}$, i.e., Taylor, 1998) records much lower temperatures compared to the $T_{REE}$ thermometer (average $\Delta T$ ~300°C), consistent with previous data on modern and ophiolitic peridotites from MOR setting (Dygert & Liang, 2015; Dygert et al., 2017; Liang et al., 2013). $T_{BKN}$ and $T_{Ta}$ yield large and comparable temperature intervals for the lherzolites ($T_{BKN}$ = 776–993°C; $T_{Ta}$ = 758–1026°C), with the lowest temperatures registered by BAB2B sample. By contrast, $T_{BKN}$ obtained for the mafic and ultramafic intrusives (Tables 2 and 3) are indicative of higher equilibrium temperatures ($T_{BKN}$ = 964–1083°C; $T_{Ta}$ = 942–1092°C).

Among cation exchange thermometers, Ca-in-orthopyroxene ($T_{Ca-in-Opx}$, i.e., Brey & Köhler, 1990) records the highest temperatures for the peridotites (lherzolites: $T_{Ca-in-Opx}$ = 1010–1082°C; harzburgites: $T_{Ca-in-Opx}$ = 903–1185°C). Ca-in-olivine ($T_{Ca-in-Ol}$, i.e., De Hoog et al., 2010) and olivine-spinel Fe-Mg thermometer ($T_{Ol-Sp}$, i.e., Li et al., 1995) indicate similar equilibrium temperatures for the peridotites (lherzolites: $T_{Ca-in-Ol}$ = 824–893°C, $T_{Ol-Sp}$ = 794–950°C; harzburgites: $T_{Ca-in-Ol}$ = 741–938°C, $T_{Ol-Sp}$ = 815–1007°C).

For the mafic-ultramafic sequence, $T_{Ca-in-Opx}$ varies between 889–1147°C (see Tables 2 and 3), with temperatures shifted toward slightly higher values

in the ultramafic lithologies (average $T_{Ca\text{-}in\text{-}Opx}$ = 1064°C) with respect to the gabbronorites (1021°C). Lower temperatures are provided by Ca-in-olivine and olivine-spinel Fe-Mg thermometers ($T_{Ca\text{-}in\text{-}Ol}$ = 684–899°C; $T_{Ol\text{-}Sp}$ = 839–982°C, see Tables 2 and 3).

Calculated $T_{REE\text{-}Y}$ were plotted against $T_{BKN}$, $T_{Ca\text{-}in\text{-}Opx}$ and $T_{Ol\text{-}Sp}$ for the lherzolites (Figures 4a–4c). In the variation diagrams, the lherzolites invariably plot far above the 1:1 line, partially overlapping the field of abyssal peridotites and the hottest ophiolitic peridotites. Plagioclase-bearing lithologies appear hotter on average, falling outside the field of the abyssal peridotites. The relationships occurring between $T_{REE}$ and mineral composition are illustrated in Figure S4 in Supporting Information S1. No correlation can be observed between $T_{REE}$ and the fertility indicators, that is, olivine Mg# or spinel Cr# (Figures S4a–S4b in Supporting Information S1), in agreement with previous observations on mantle peridotites (Dygert & Liang, 2015; Dygert et al., 2017).

By contrast, a weak positive correlation is displayed by $T_{REE}$ and orthopyroxene Ca contents (Figure S4c in Supporting Information S1), possibly reflecting temperature-sensitive Ca partitioning around the enstatite-diopside solvus.

## 5. Discussion

### 5.1. Origin and Cooling History of the Northern Peridotite Massifs

Spinel- and plagioclase-bearing lherzolites from New Caledonia provide comparable equilibration temperatures, suggesting similar cooling histories (see Table 1).

The lherzolites from Poum and Babouillat yield some of the highest $T_{REE\text{-}Y}$ ever reported for ophiolites and abyssal peridotites (e.g., Dygert & Liang, 2015). Among the studied samples, the highest $T_{REE\text{-}Y}$ (up to ∼1400°C) were recorded by two plagioclase-bearing lithologies (BAB2A-BAB2B). Similar high temperatures are often registered by plagioclase-impregnated peridotites. The anomalously high T have been tentatively attributed to REE + Y disequilibrium partitioning between the two pyroxenes, due to reactive melt percolation (Dygert & Liang, 2015; Liang et al., 2013).

To quantify the cooling rates experienced by the studied rock types, we have applied the method of Dygert and Liang (2015) and Dygert et al. (2017). Figure 4d illustrates closure curves built using a modified form of Dodson's equation (Ganguly & Tirone, 1999), which models the dependence of closure temperature (Tc) on grain size, initial temperature, and cooling rate, assuming the closure of $T_{REE}$ are rate-limited by diffusion of REEs in orthopyroxene (Cherniak & Dimanov, 2010) and the closure of $T_{BKN}$ are approximated by diffusion of Fe-Mg in clinopyroxene (Dimanov & Wiedenbeck, 2006). Red lines in Figure 4d represent cooling curves for one-stage cooling starting at peak temperature ($T_0$), presumably along the solidus, to final closure temperatures for $T_{REE}$ and $T_{BKN}$, depending on cooling rate (vertical black lines). Cooling curves have been calculated for a grain radius of 2.5 mm, that is, the average grain size obtained through petrographic observations.

In Figure 4d, BA1, BAB1B and POU2 lherzolite samples plot in a region typical of abyssal peridotites and mid-ocean ridge ophiolites (such as Corsica and Oman, e.g., Dygert et al., 2017), whereas the other plagioclase lherzolites (BAB2A, BAB2B and POU1A) fall outside the cooling curves, lying at the top left. Samples falling in this area in cooling diagrams are believed to reflect thermal disturbance related to melt-rock reactions or complex thermal histories (i.e., early cooling followed by re-heating, e.g., Dygert & Liang, 2015; Dygert et al., 2017). Thus, these temperatures cannot be considered as representative of the thermal state of the lherzolite massifs.

Results for BA1, BAB1B and POU2 samples are consistent with cooling from asthenospheric temperatures of 1400°C and 1300°C, respectively, at cooling rates of ≈$4 \times 10^{-3}$°C/yr. These cooling rates are similar to those registered by other ophiolitic mantle sections (i.e., Canil et al., 2019; Dygert & Liang, 2015; McGoldrick et al., 2018), but slightly higher compared to those reported for SSZ peridotites (∼$10^{-6}$–$10^{-4}$°C/y, see Dygert & Liang, 2015). Intriguingly, these values tend to be somewhat lower compared to the cooling rates registered by the Wadi Tayin mantle (i.e., Oman, see Dygert et al., 2017), which is overlapped by a 5–7 km thick crustal sequence. This observation supports the suggestion of Dygert et al. (2017) that cooling of the oceanic mantle is not governed by the thickness of overlying crust in any systematic way.

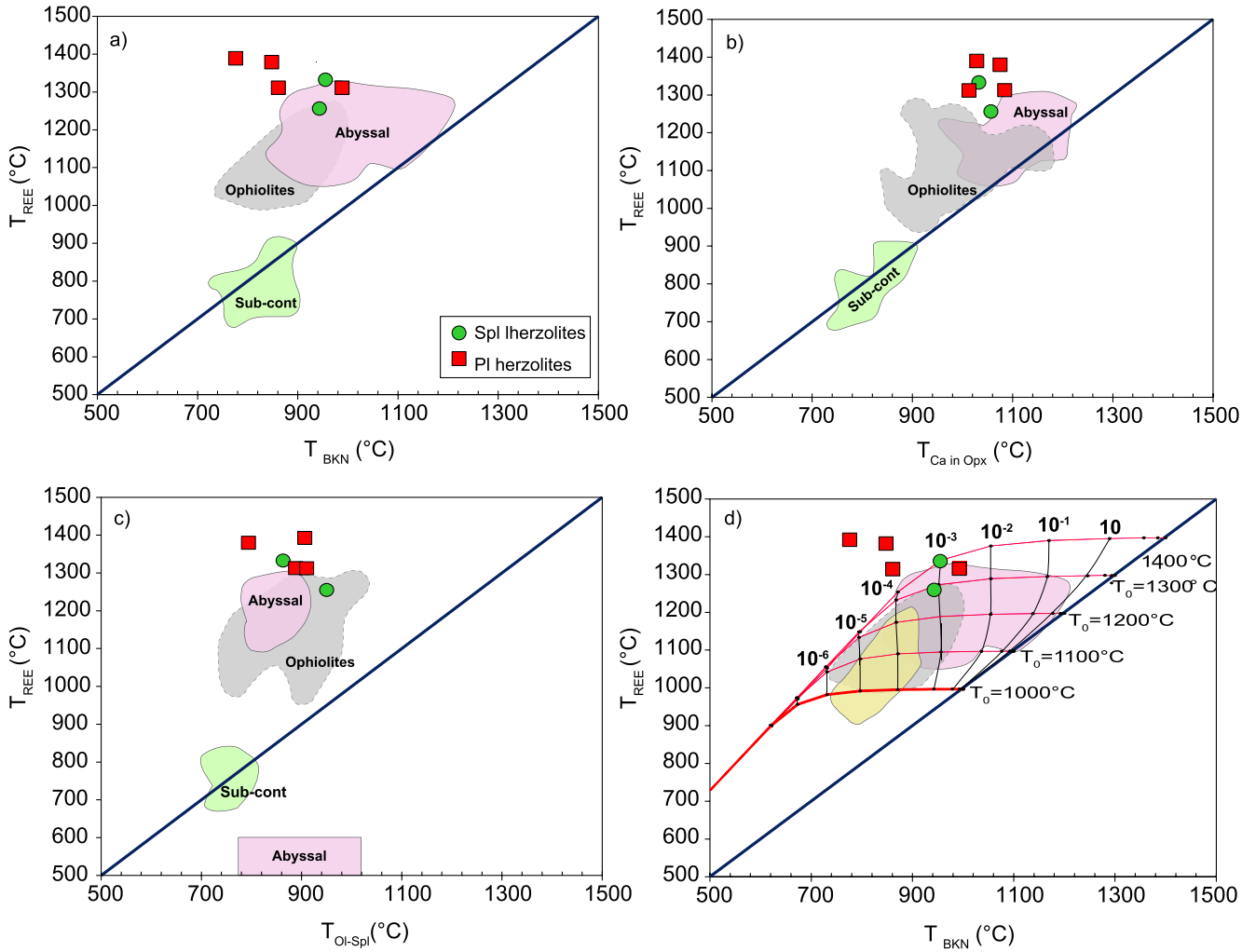


**Figure 4.** Comparison of temperatures derived from the REE-in-two-pyroxene thermometer ($T_{REE\text{-}Y}$, Liang et al., 2013) with temperatures from (a) two-pyroxene thermometer ($T_{BKN}$, Brey & Köhler, 1990); (b) Ca-in-orthopyroxene thermometer ($T_{Ca\text{-}in\text{-}Opx}$, Brey & Köhler, 1990) and (c) olivine-spinel thermometer ($T_{Ol\text{-}Spl}$, Li et al., 1995). (4d): diagram showing closure temperature cooling curves (red lines) calculated for initial peak temperatures on the solidus ($T_0$) followed by cooling at various rates (in °C/year-vertical black lines) to the final closure temperatures of $T_{REE}$ and $T_{BKN}$ for an average 2.5 mm grain radius of orthopyroxene. The calculations follow the method and diffusion parameters for REE and Fe-Mg diffusion in pyroxenes outlined in Dygert et al. (2017). Pink and light gray fields represent abyssal and ophiolitic peridotites, respectively, from Dygert et al. (2017). Light yellow field: supra-subduction zone peridotites (Canil et al., 2019).

The cooling rates deduced for the New Caledonia lherzolites also cover the same range of values of the oceanic lower crustal lithosphere dominated by conductive cooling (e.g., Coogan et al., 2002; Dygert et al., 2017; Faak & Gillis, 2016), in contrast to lithospheric sections re-equilibrated through hydrothermal circulation, which generally yield cooling rates one or two orders of magnitude higher ($\approx 10^{-2}$ or $10^{-1}$°C/y, e.g., Dygert et al., 2017; VanTongeren et al., 2008).

For spinel lherzolites BA1 and POU2, melting temperatures were also computed using the method proposed by Lee and Chin (2014), which is based on bulk MgO, $FeO_t$, and $SiO_2$ contents. Temperatures for anhydrous melting are in good agreement with peak temperatures obtained with the method of Dygert and Liang (2015) for spinel lherzolites ($T = 1383$°C for BA1 and $T = 1410$°C for POU2), lying in the range of most abyssal peridotites (Lee & Chin, 2014).

Temperatures calculated with other geothermometers exhibit a smooth and systematic decrease in the order: $T_{Ca\text{-}in\text{-}Opx}$, $T_{Ta}$ and $T_{BKN}$, $T_{Ol\text{-}Sp}$ and $T_{Ca\text{-}in\text{-}Ol}$. This systematic decrease can be related to the different diffusion rates of the various elements (or components) used to calibrate the thermometers (Chakraborty, 2010; Cherniak & Dimanov, 2010).

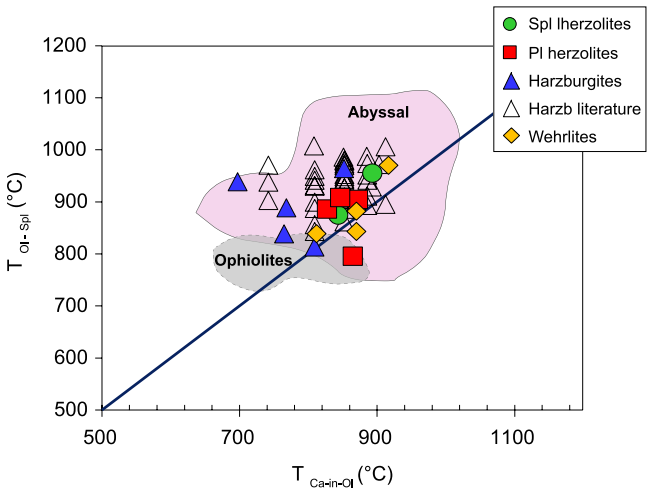


**Figure 5.** Results of $T_{Ca\text{-}in\text{-}Ol}$ (De Hoog et al., 2010) plotted against $T_{Ol\text{-}Sp}$ (Li et al., 1995). Field of abyssal peridotites includes data from Warren (2016). New Caledonia samples: spinel and plagioclase lherzolites (Secchiari et al., 2016); harzburgites (Secchiari et al., 2020); literature harzburgites (Marchesi et al., 2009; Pirard et al., 2013; Xu et al., 2020); wehrlites (Marchesi et al., 2009; Pirard et al., 2013). Data sources for ophiolites: Aldanmaz (2012); Barth et al. (2003); Batanova et al. (2011); Dygert and Liang (2015); Dygert et al. (2016); Jean et al. (2010); Khedr et al. (2014); Marchesi et al. (2011); Müntener et al. (2010); Riches and Rogers (2011); Takazawa et al. (2003).

Major element-based thermometers for Poum and Babouillat lherzolites record temperatures in the range of abyssal and ophiolitic peridotites from MOR setting (Table 1, Figure 5), similar to $T_{REE\text{-}Y}$ estimates.

To assess how cooling proceeds at lower temperature conditions, cooling rates from Ca-in-olivine thermometry were computed for the investigated samples assuming an average grain radius of 1 mm, as indicated from petrographic investigations. The calculated values provide consistent results for all the lherzolites, in the range of $\approx 10^{-3}$°C/y. Remarkably, these cooling rates are comparable to those recorded by $T_{REE\text{-}Y}$ and $T_{BKN}$ at higher temperature intervals.

We propose that the similarities between the abyssal peridotites and the New Caledonia lherzolites mirror an evolution in a marginal basin predating Eocene subduction, followed by fast uplift and emplacement. Such fast emplacement possibly occurred along a transform fault (Prinzhofer & Nicolas, 1980; Titus et al., 2011), in agreement to what was previously proposed by Secchiari et al., (2016) based on the melting history of the lherzolites. Notably, the presence of a major shear zone, running along the northeastern side of the Belep Islands and Poum and Tiebaghi massifs, has been reported for many years by Nicolas (1989), who interpreted this high-strain zone as a paleo-transform fault (Nicolas, 1989).

The similar cooling rates, in the range of $10^{-3}$°C/y, recorded through the high and lower temperature intervals also suggest that cooling and thermal re-equilibration must have continued at constant rates throughout the whole post-melting evolution of the lherzolite massif, and possibly by conduction.

### 5.2. Thermal Evolution of the Ultra-depleted Harzburgites

Due to the lack of primary clinopyroxene, high-temperature constraints for the New Caledonia harzburgites are difficult to obtain.

Despite the fact that two pyroxene exchange thermometers cannot be applied to constrain cooling of the harzburgites from peak temperature, temperature estimates can still be obtained using orthopyroxene major element compositions. These values represent minimum temperatures under the assumption that orthopyroxene composition reflects equilibrium with clinopyroxene. This appears reasonable, as cooling of an initially clinopyroxene-undersaturated orthopyroxene and subsolidus exchange of Ca with olivine will result in clinopyroxene saturation (Lindsley, 1983). Notably, clinopyroxene exsolution lamellae are widely observed within porphyroclastic orthopyroxene in the analyzed harzburgites. As a whole, $T_{Ca\text{-}in\text{-}Opx}$ computed for the investigated samples are relatively high and homogeneous, giving an average $T_{Ca\text{-}in\text{-}Opx}$ = 1020°C. The calculated range of values ($T_{Ca\text{-}in\text{-}Opx}$ = 903–1185°C) appear wider and shifted towards slightly higher values than temperatures reported by Pirard et al. (2013) for the same lithologies ($T_{Ca\text{-}in\text{-}Opx}$ = 953–970°C), falling in the range of abyssal and other subduction-related peridotites (Dygert & Liang, 2015; Dygert et al., 2017). Notably, the lower temperature interval (903–923°C) is mainly covered by the mylonitic harzburgites from the Ouassè bay (Table 1). Such low temperatures are likely related to deformation along the Bogota shear zone (Titus et al., 2011), which produced mylonitic textures and overall grain size reduction. Alternatively, the lower temperatures preserved by these harzburgites may reflect a shear heating temperature, overwriting the previous thermal history. For the Bogota mylonites, the occurrence of orthopyroxene neoblasts providing equilibrium temperatures similar to the coexisting porphyroclasts ($T_{Ca\text{-}in\text{-}Opx}$ = 923–945°C, Ferrari et al., 2021) supports the hypothesis that thermal re-equilibration of orthopyroxene porphyroclasts occurred after shearing and grain size reduction. Further constraints on the subsolidus thermal evolution of the harzburgites are provided by Ca in olivine ($T_{Ca\text{-}in\text{-}Ol}$) and olivine-spinel geothermometers ($T_{Ol\text{-}Sp}$). As these thermometers are based on the exchange of relatively fast-diffusing mineral components, their application offers crucial insights on the last cooling stages of mantle peridotites, as well as on the emplacement mechanisms of the peridotite massifs. In particular, the equilibrium exchange of

**Table 2**
*Equilibrium Temperatures and Cooling Rates Calculated for the New Caledonia Mafic and Ultramafic Intrusives*

| Sample | Locality | Lithology | Note | Source | P (kbar) | $T_{Pl\text{-}Cpx}$ | 1σ | $T_{BKN}$ | $T_{Ta}$ | $T_{Ca\text{-}in\text{-}Opx}$ | $T_{Ca\text{-}in\text{-}Ol}$ | $T_{Ol\text{-}Sp}$ | Ol radius (mm)[c] | dT/dt (°C/y) from $T_{Ca\text{-}in\text{-}Ol}$ |
|---|---|---|---|---|---|---|---|---|---|---|---|---|---|---|
| CDM1[a] | Col de Mouirange | Wehrlite | Cumulate | Secchiari et al., this work | 3 | – | – | – | – | 889 | – | 877 | – | – |
| CDM2 | Col de Mouirange | Spl dunite | Cumulate | Secchiari et al., this work | – | – | – | – | – | – | – | 844 | – | – |
| CDM3 | Col de Mouirange | Gabbronorite | Cumulate | Secchiari et al. (2018) | 2 | – | – | – | – | – | 730 | – | 0.5 | 4.66E−04 |
| CDM6 | Col de Mouirange | Gabbronorite | Cumulate | Secchiari et al. (2018) | 2 | – | – | – | – | – | 707 | – | 0.5 | 2.49E−04 |
| PL1[a] | Plum | Gabbronorite | Cumulate | Secchiari et al. (2018) | 1.9[b] | 1241 | 43 | – | – | 926 | 734 | – | 0.5 | 5.19E−04 |
| PR2B | Rivière des Pirogues | Gabbronorite | Cumulate | Secchiari et al. (2018) | 2 | – | – | – | – | – | 730 | – | 0.5 | 4.66E−04 |
| PR3[a] | Rivière des Pirogues | Gabbronorite | Cumulate | Secchiari et al. (2018) | 2 | 1243 | 23 | – | – | 980 | 718 | – | 0.5 | 3.37E−04 |
| PR4 | Rivière des Pirogues | Ol clinopyroxenite | Cumulate | (Secchiari et al., this work | – | – | – | – | – | – | – | 942 | – | – |
| PRO3b | Prony | Gabbronorite | Cumulate | Secchiari et al. (2016) | 2.8[b] | – | – | 1054 | 1030 | 1040 | – | 866 | – | – |
| PR 1B[a] | Prony | Opx-gabbronorite | | Marchesi et al. (2009) | 2 | – | – | – | – | 1066 | 819 | – | 0.5 | 4.18E−03 |
| PR3A | Prony | Opx-gabbronorite | | Marchesi et al. (2009) | 2 | – | – | 964 | 957 | 925 | 684 | – | 0.5 | 1.29E−04 |
| MS36 | Montagne des Sources | Pl-dunite | | Marchesi et al. (2009) | – | – | – | – | – | – | – | 904 | – | – |
| MS20 | Montagne des Sources | Pl-Wehrlite | | Marchesi et al. (2009) | 3.2[b] | – | – | 967 | 942 | 1087 | 853 | 886 | 0.8 | 3.45E−03 |
| MS22 | Montagne des Sources | Pl-Wehrlite | | Marchesi et al. (2009) | 3.0[b] | – | – | 1008 | 967 | 1114 | 796 | 839 | 0.8 | 9.58E−04 |
| MS28[a] | Montagne des Sources | Pl-Wehrlite | | Marchesi et al. (2009) | 3 | – | – | – | – | 1055 | 853 | – | 0.8 | 3.46E−03 |
| MS30[a] | Montagne des Sources | Pl-Wehrlite | | Marchesi et al. (2009) | 3 | – | – | – | – | 1099 | 853 | – | 0.8 | 3.46E−03 |
| MS31[a] | Montagne des Sources | Pl-Wehrlite | | Marchesi et al. (2009) | 3 | – | – | – | – | 1105 | 827 | – | 0.8 | 1.98E−03 |
| MS32[a] | Montagne des Sources | Pl-Wehrlite | | Marchesi et al. (2009) | 3 | – | – | – | – | 1036 | 853 | 844 | 0.8 | 3.45E−03 |
| MS35 | Montagne des Sources | Opx-gabbronorite | | Marchesi et al. (2009) | 2 | – | – | 1034 | 1019 | 1110 | – | – | – | – |
| MS37 | Montagne des Sources | Cpx-dunite | | Marchesi et al. (2009) | – | – | – | – | – | – | – | 880 | – | – |
| MS38 | Montagne des Sources | Dunite | | Marchesi et al. (2009) | – | – | – | – | – | – | – | 884 | – | – |
| MS39 | Montagne des Sources | Dunite | | Marchesi et al. (2009) | – | – | – | – | – | – | – | 856 | – | – |
| MS40 | Montagne des Sources | Dunite | | Marchesi et al. (2009) | – | – | – | – | – | – | – | 964 | – | – |
| MDS34[a] | Montagne des Sources | Wehrlite | Cumulate | Pirard et al. (2013) | 3 | – | – | – | – | 1147 | 899 | 970 | 0.8 | 8.91E−03 |
| MDS37 | Montagne des Sources | Gabbro | Cumulate | Pirard et al. (2013) | 2.4[b] | – | – | 1074 | 1050 | 1101 | 869 | – | 0.5 | 1.24E−02 |

**Table 2**
*Continued*

| Sample | Locality | Lithology | Note | Source | P (kbar) | $T_{Pl\text{-}Cpx}$ | 1σ | $T_{BKN}$ | $T_{Ta}$ | $T_{Ca\text{-}in\text{-}Opx}$ | $T_{Ca\text{-}in\text{-}Ol}$ | $T_{Ol\text{-}Sp}$ | Ol radius (mm)[c] | dT/dt (°C/y) from $T_{Ca\text{-}in\text{-}Ol}$ |
|---|---|---|---|---|---|---|---|---|---|---|---|---|---|---|
| MDS43 | Montagne des Sources | Dunite | Cumulate | Pirard et al. (2013) | – | – | – | – | – | – | – | 982 | – | – |
| MDS49 | Montagne des Sources | Dunite | Cumulate | Pirard et al. (2013) | 3 | – | – | – | – | – | – | 886 | – | – |
| RP33 | Rivière des Pirogues | Websterite | Cumulate | Pirard et al. (2013) | 3 | – | – | 1087 | 1081 | 990 | – | – | – | – |
| RP51 | Rivière des Pirogues | Clinopyroxenite | Cumulate | Pirard et al. (2013) | 3 | – | – | 1028 | 1092 | 1117 | – | – | – | – |

*Note*. $T_{Pl\text{-}Cpx}$ = REE-Y in plagioclase-clinopyroxene pair (Sun & Liang, 2017); $T_{BKN}$ - $T_{Ta}$ = two-pyroxene solvus thermometers (Brey & Köhler, 1990; Taylor, 1998); $T_{Ca\text{-}in\text{-}Opx}$ = Ca in orthopyroxene thermometer (Brey & Köhler, 1990); $T_{Ca\text{-}in\text{-}Ol}$ = Ca in olivine thermometer (De Hoog et al., 2010); $T_{Ol\text{-}Sp}$ = olivine-spinel Fe-Mg thermometer (Li et al., 1995). T were computed using averaged composition of crystal cores.

[a]Cpx-free mafic and ultramafic intrusives: for these samples $T_{Ca\text{-}in\text{-}Opx}$ represent minimum temperature estimates under the assumption that orthopyroxene composition reflects equilibrium with clinopyroxene. [b]Pressure calculated following the method of Fumagalli et al. (2017). [c]Olivine grain radius = average olivine grain radius used for calculations of cooling rates based on $T_{Ca\text{-}in\text{-}Ol}$. Olivine grain radius was deduced from petrographic observations for samples from Secchiari et al. (2018). For the other literature works (Marchesi et al., 2009; Pirard et al., 2013) an average olivine grain radius of 0.5 and 0.8 mm was assumed for the gabbronorites and the wehrlites, respectively.

$Mg^{2+}$ and $Fe^{2+}$ between olivine and spinel represents the fastest exchange and continues during cooling down to relatively low temperatures (~500°C, e.g., Fabriès, 1979). Hence, the olivine-spinel geothermometer yields the temperatures of the last stages of equilibration, when an equilibrium state is almost reached or exchange reactions are blocked by cooling.

Temperatures calculated with $T_{Ca\text{-}in\text{-}Ol}$ thermometer for the New Caledonia harzburgites cover a wide range of values (741–938°C, average $T_{Ca\text{-}in\text{-}Ol}$ = 842°C, see Tables 1 and 3), mirroring the variable Ca contents of olivine (Table S3).

Olivine-spinel geothermometer records even higher temperatures compared to Ca-in-olivine thermometer, bearing values up to 1000°C, with an average of $T_{Ol\text{-}Sp}$ = 924°C. As a whole, the harzburgites exhibit remarkably higher equilibrium temperatures for the fast diffusing thermometers (Figure 5) in comparison to all ophiolitic - both from supra-subduction zone and MOR setting-and modern arc peridotites, plotting in the field of modern abyssal mantle. This observation represents an interesting contrast with the previous results on obducted ophiolitic peridotites (e.g., Dygert et al., 2017; Hanghøj et al., 2010), for which slower cooling than abyssal peridotites is generally observed (Canil et al., 2019; Dygert et al., 2017), possibly as a result of hydrothermal cooling cessation after obduction.

To gain additional insights into the thermal history of the harzburgites, we computed cooling rates using Ca-in-olivine thermometer. For this calculation, we used an olivine grain radius of 0.8 mm for the harzburgites from the central peridotite massifs, while 1 mm radius was chosen for the sample from Yaté (YA1), based on petrographic observations. For the other samples from literature, a grain radius of 1 mm was assumed. This approximation is reasonable, as most of the studied harzburgites were sampled in the Massif du Sud area, close to our YA1 sample. The calculated cooling rates yield similar values for all the investigated harzburgites, in the range of $10^{-4}$–$10^{-3}$°C/y. These results are comparable with those obtained for the northern lherzolites, falling in the range of the oceanic lithosphere that cooled via conduction (e.g., Coogan et al., 2002).

Previous studies have shown that, among mantle rocks, forearc peridotites generally register the lowest equilibration temperatures (Ohara & Ishii, 1998; Parkinson & Pearce, 1998; Zanetti et al., 2006). These thermal features were interpreted to reflect long cooling histories, dominated by low heat extraction rates, in presence of water (e.g., Dygert & Liang, 2015).

In order to unveil the meaning of the atypical thermal state recorded by the investigated lithotypes, the geodynamic evolution of the New Caledonia archipelago needs to be taken into account. Geodynamic models indicate that New Caledonia experienced a phase of marginal basin formation starting from Campanian to Paleocene, followed

**Table 3**
*Summary of the Temperatures Recorded by the Main Lithologies Belonging to the New Caledonia Nappe*

| Lithology | $T_{REE}$ min | $T_{REE}$ max | $T_{BKN}$ min | $T_{BKN}$ max | $T_{BKN}$ average | $T_{Ta}$ min | $T_{Ta}$ max | $T_{Ta}$ average | $T_{Ca\text{-}in\text{-}Opx}$ min | $T_{Ca\text{-}in\text{-}Opx}$ max | $T_{Ca\text{-}in\text{-}Opx}$ average | $T_{Ca\text{-}in\text{-}Ol}$ min | $T_{Ca\text{-}in\text{-}Ol}$ max | $T_{Ca\text{-}in\text{-}Ol}$ average | $T_{Ol\text{-}Sp}$ min | $T_{Ol\text{-}Sp}$ max | $T_{Ol\text{-}Sp}$ average |
|---|---|---|---|---|---|---|---|---|---|---|---|---|---|---|---|---|---|
| Lherzolites | 1256 | 1394 | 776 | 993 | 896 | 758 | 1026 | 1046 | 1010 | 1082 | 1046 | 824 | 893 | 855 | 794 | 950 | 885 |
| Harzburgites[a] | – | – | – | – | – | – | – | – | 903 | 1185 | 1020 | 741 | 938 | 842 | 815 | 1007 | 924 |
| Mafic-ultramafic intrusives | – | – | 964 | 1083 | 1027 | 942 | 1092 | 1017 | 889 | 1147 | 1046 | 684 | 899 | 795 | 839 | 982 | 898 |
| Mafic intrusives[b] | 1241 | 1243 | 964 | 1050 | 1014 | 957 | 1050 | 1014 | 925 | 1110 | 1021 | 684 | 819 | 732 | – | – | – |
| Ultramafic intrusives[c] | – | – | – | – | – | – | – | – | 889 | 1147 | 1064 | 796 | 899 | 850 | 839 | 982 | 898 |
| Dunites | – | – | – | – | – | – | – | – | – | – | – | – | – | – | 844 | 964 | 906 |

*Note*. $T_{REE}$ indicates REE-Y-in-two-pyroxene thermometer (Liang et al., 2013) for the lherzolites and clinopyroxene-plagioclase thermometer (Sun & Liang, 2017) for the mafic intrusives (i.e., gabbronorites); $T_{BKN}$-$T_{Ta}$ = two-pyroxene solvus thermometers (Brey and Köhler, 1990; Taylor, 1998); $T_{Ca\text{-}in\text{-}Opx}$ = Ca in orthopyroxene thermometer (Brey & Köhler, 1990); $T_{Ca\text{-}in\text{-}Ol}$ = Ca in olivine thermometer (De Hoog et al., 2010); $T_{Ol\text{-}Sp}$ = olivine-spinel Fe-Mg thermometer (Li et al., 1995).
[a]Cpx-free harzburgites: for these samples $T_{Ca\text{-}in\text{-}Opx}$ have to be considered as minimum estimates under the assumption that orthopyroxene composition reflects equilibrium with clinopyroxene. [b]Mafic intrusives = opx-gabbros and gabbronorites. [c]Ultramafic intrusives = wehrlites and pyroxenites.

by intra-oceanic subduction during Eocene (~56 Ma, Cluzel et al., 2016). It has been proposed that the Eocene subduction started close to or in correspondence of an active oceanic spreading center (Ulrich et al., 2010), where relatively hot and young lithosphere (≈6–9 Ma old, see Cluzel et al., 2016) was forced to subduct. Continued convergence finally resulted in proto arc-continent collision, which led to overthrusting of the ophiolitic units onto the Norfolk ridge ~34 Ma ago (Cluzel, Jourdan et al., 2012). In this framework, the results provided by the fast diffusing thermometers may be explained as reflecting short residence times of the depleted mantle from the forearc region (~20 Ma), followed by fast emplacement due to obduction (Aitchison et al., 1995; Cluzel, Maurizot et al., 2012a, Cluzel, Jourdan et al., 2012; Lagabrielle et al., 2013).

This conclusion challenges the general assumption that subduction-related peridotites cool over longer time intervals and possibly from lower initial temperatures (Dygert & Liang, 2015). We interpret this apparent contradiction as specifically related to the tectonic evolution of the New Caledonia archipelago, that is, to the development of an ephemeral subduction system involving a young oceanic lithosphere. Notably, the young age of the subducted lithosphere is also expected to have prevented the presence of large volumes of sediments and fluids in the subduction zone (Cluzel et al., 2016; Secchiari et al., 2020).

### 5.3. Genesis and Cooling Mechanisms of the Mafic-Ultramafic Sequence

The mineralogical variability of the New Caledonia layered mafic and ultramafic intrusives, allowed the application of several geothermometers.

In the uppermost part of the intrusive sequence, T estimates based on the REE-Y exchange between plagioclase and clinopyroxene ($T_{Pl\text{-}Cpx}$, Sun & Liang, 2017) yield high values (1241–1243°C), which are interpreted as crystallization temperatures of the gabbronorite parental melts (see also Secchiari et al., 2018). Previous studies hypothesized that the gabbronorite crystallization occurred at low-pressure conditions (~2–4 kbar, i.e., Pirard et al., 2013). These values are in good agreement with our estimates obtained using the FACE geobarometer (~2–3 kbar). The inferred depths are remarkably low compared to the crust-mantle transition of exposed arc sections (e.g., P ~10 kbar for Kohistan, Burg et al., 1998) and are consistent with magma emplacement in a thinned forearc lithosphere during subduction initiation (see also Pirard et al., 2013). Derivation from boninitic magmas was previously proposed for the New Caledonia gabbronorites (Marchesi et al., 2009; Pirard et al., 2013). However, their ultra-depleted compositions, coupled with the early appearance of plagioclase and late segregation of orthopyroxene, point to crystallization from $H_2O$-poor magmas more akin to tholeiites. More specifically, the composition of the parental melts in equilibrium with the New Caledonia gabbronorites was shown to significantly diverge from boninitic melts in having lower LREE-MREE (i.e., light and medium rare earth elements) and FME (i.e., fluid mobile elements) contents, no Nb depletion, and in the lack of Zr -Hf positive anomalies (Secchiari et al., 2018). Notably, $T_{Pl\text{-}Cpx}$ (Sun & Liang, 2017) obtained in this study appear ~150°C lower than temperatures experimentally determined by Falloon and Danyushevsky (2000) for boninitic melts.

Other insights concerning the thermal evolution of the gabbronorites can be obtained from Ca-in-Opx and two pyroxene Fe-Mg thermometers. $T_{Ca\text{-}in\text{-}Opx}$ (925–1110°C; average $T_{Ca\text{-}in\text{-}Opx}$ = 1021°C) mainly fall in the range of the two-pyroxene thermometer estimates (see Table 3). As a whole, pyroxene thermometry give considerably lower temperatures compared to $T_{Pl\text{-}Cpx}$ ($\Delta T \sim 200$°C), which can be ascribed to higher diffusion rates of divalent cations with respect to trivalent REE. $T_{Ca\text{-}in\text{-}Opx}$ and two pyroxene Fe-Mg thermometers thus depict the subsolidus evolution of the gabbronorites.

Major element pyroxene thermometry was also applied to the ultramafic rocks from the base of the layered intrusive lenses of the New Caledonia ophiolite (i.e., wehrlites, pyroxenites and some dunites, see Tables 2 and 3). For these rock types, the calculated $T_{Ca\text{-}in\text{-}Opx}$ and $T_{BKN}$ provide similar values to the overlying gabbronorites, with an average 1064°C and 1023°C, respectively (Table 3).

On the other hand, an upward decrease of $T_{Ca\text{-}in\text{-}Ol}$ is recorded from the wehrlites (796–899°C, average $T_{Ca\text{-}in\text{-}Ol}$ = 850°C) and the gabbronorites (684–819°C, average $T_{Ca\text{-}in\text{-}Ol}$ = 732°C), mirroring the higher Ca contents of the ultramafic rocks (up to ≈ 500 ppm for the wehrlites, see Table S3). By contrast, the extreme Ca contents shown by the dunites (up to 1800 ppm, see Table S3), possibly reflect the lack of sub-solidus equilibrium, owing to the absence of pyroxene (Pirard et al., 2013). Thus, $T_{Ca\text{-}in\text{-}Ol}$ for the dunites cannot be assumed as representative of their cooling state and were not considered. Information on the subsolidus history of the dunites can only be obtained using the olivine-spinel geothermometer, which records similar temperatures compared to the other ultramafic lithologies (average $T_{Ol\text{-}Sp}$ = 906°C and 898°C for the dunites and wehrlites-pyroxenites, respectively) and to the only spl-bearing gabbronorite sample included in our data set ($T_{Ol\text{-}Sp}$ = 866°C). As a whole, $T_{Ca\text{-}in\text{-}Ol}$ and $T_{Ol\text{-}Sp}$ are high and homogeneous for the mafic-ultramafic cumulates, falling in the range of the New Caledonia harzburgites and abyssal peridotites (Figure 5).

To better constrain the thermal history of the mafic-ultramafic sequence, olivine cooling rates were also computed for the gabbronorites and the wehrlites. An olivine grain radius of 0.5 mm was used for the gabbronorites from Secchiari et al., (2018). The same grain size was assumed for the gabbronorites and Opx-gabbros from literature, while we chose an olivine grain size of 0.8 mm for the wehrlites, as petrographic observations generally revealed a coarser grain size for these lithotypes. Our results indicate cooling rates of $\approx 10^{-4}$°C/y for the gabbronorites (except PR1B sample, which shows a higher cooling rate, $\approx 10^{-3}$) and $10^{-3}$°C/y for the wehrlites (Table 2). One gabbronorite sample (MDS37) exhibits remarkably higher cooling rates ($\approx 10^{-2}$°C/y) compared to the other mafic-ultramafic rocks in our data set. However, this value is several orders of magnitude higher compared to the other gabbronorites from the same locality. Thus, we believe that this high value possibly derived from a wrong assumption of the olivine grain size, rather than being representative of the real cooling rate experienced by the gabbronorites.

To assess temperature variations with depth across the Massif du Sud sequence, average closure temperatures for each geothermometer were reported for the mafic-ultramafic cumulates and the underlying tectonite harzburgite (Figure 6). This allows us to build, even if in a qualitative way, temperature profiles from the lower crust to the mantle, passing through the Moho transition zone. As it can be observed, temperature variation with depth appears limited, with the various geothermometers mostly showing high and constant temperatures moving from the lower crust (i.e., the gabbronorites) to the depleted peridotite. Likewise, the cooling rates estimated from Ca-in-olivine thermometer mirror the trend shown by the various geothermometers, displaying limited variations from the lower crust to the tectonite harzburgite.

Recent geochemical works proposed that the New Caledonia mafic-ultramafic sequence originated in a nascent intra-oceanic arc, from multiple, non-cogenetic, magma batches bearing a depleted supra-subduction zone signature (Marchesi et al., 2009; Pirard et al., 2013; Secchiari et al., 2018). From this perspective, we are prone to interpret our results as reflecting the emplacement of hot, depleted magma batches in a young forearc lithosphere, as supported by the high $T_{Pl\text{-}Cpx}$, followed by cooling and sub-solidus re-equilibration.

The similar thermal conditions and cooling rates hint that the mafic-ultramafic sequence, together with the depleted forearc mantle, experienced a similar history of cooling and thermal re-equilibration at lower temperatures. In particular, the high equilibrium temperatures computed with the fast diffusing geothermometers, in the range of modern abyssal peridotites, are atypical in a forearc region and strikingly contrast with the previous results for this geodynamic setting. The thermal signature preserved by the New Caledonia ophiolite likely reflects its

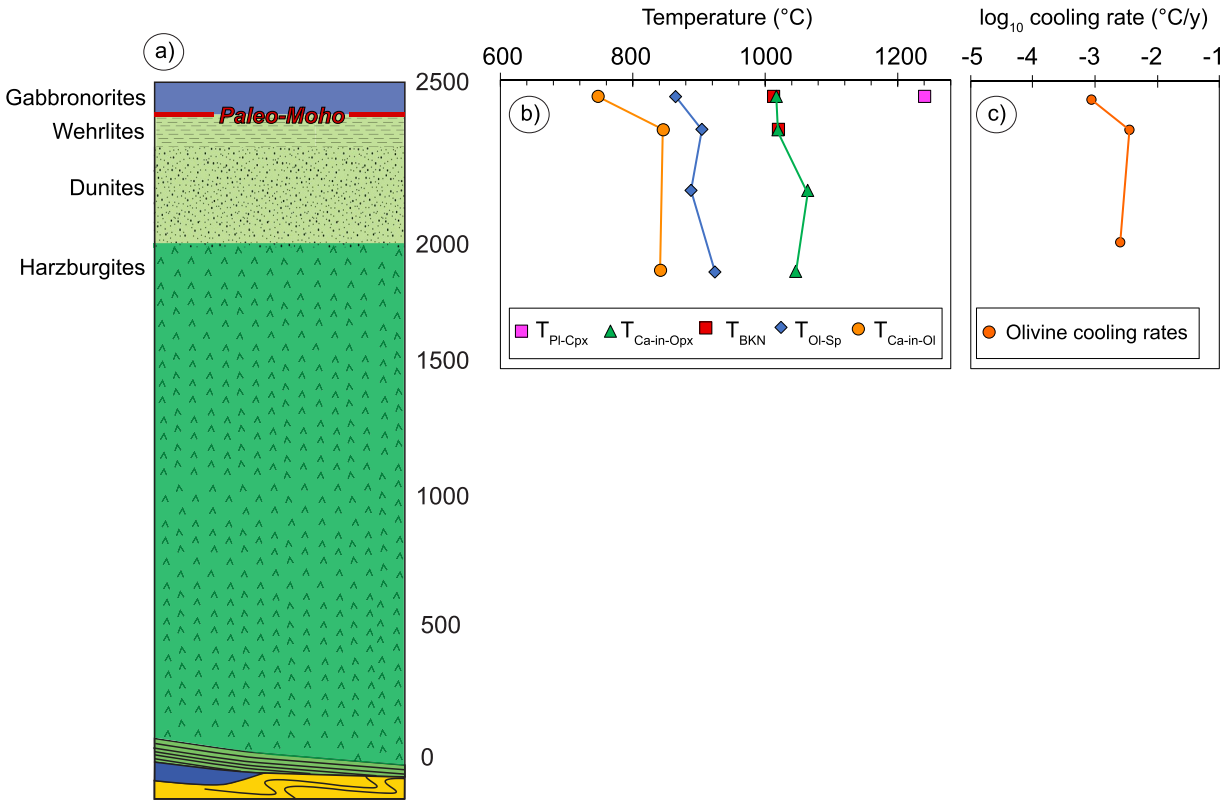


**Figure 6.** (a) Simplified schematic representation of the stratigraphy in the Massif du Sud sequence; (b) temperature profiles and (c) olivine cooling rates extending from the lower crust to the depleted mantle. Temperatures profiles were built using average temperature values for each geothermometer. Olivine cooling rates are reported as average cooling rates for each lithology (i.e., gabbronorites, wehrlites and harzburgites).

geodynamic evolution, that is, the development of an ephemeral subduction, suddenly followed by obduction and emplacement of the ophiolitic units (Cluzel, Maurizot et al., 2012).

For the Ca-in-olivine thermometer, slightly lower equilibrium temperatures, coupled to lower olivine cooling rates, are recorded by some gabbronorites compared to the underlying wehrlites. However, these variations appear limited and were possibly related to disturbance of the Ca-in-olivine thermometer, perhaps due to re-heating beyond Ca in olivine closure temperature.

Unfortunately, the lack of geothermometric studies carried out in complete sequences from forearc setting prevents any comparison with similar crust-mantle transects (Dygert & Liang, 2015). This can be reconciled with the rare occurrence of complete forearc sections in ophiolites (e.g., Greene, 2006; Garrido et al., 2007), as well as the difficulty in accessing complete crustal sequences in modern forearc environments.

## 6. Summary and Concluding Remarks

In this work, we present the first detailed geothermometric investigation carried out in a young forearc sequence originated during subduction inception. To unravel how the oceanic lithosphere cools in this poorly investigated geodynamic setting, various chemical thermometers (i.e., $T_{REE\text{-}Y}$, $T_{Ca\text{-}in\text{-}Opx}$, $T_{BKN}$, $T_{Ca\text{-}in\text{-}Ol}$, $T_{Ol\text{-}Sp}$, $T_{Pl\text{-}Cpx}$) were applied to peridotite and mafic-ultramafic cumulates from the New Caledonia ophiolite. Cooling rates, using combined $T_{REE\text{-}Y}$ and $T_{BKN}$ , and $T_{Ca\text{-}in\text{-}Ol}$, were also computed.

Equilibrium temperatures calculated for the lherzolites indicate that spinel- and plagioclase-bearing lithologies experienced similar thermal histories. $T_{REE\text{-}Y}$ computed for the lherzolites from Poum and Babouillat areas are among the highest ever documented for ophiolitic peridotites (1256–1334°C), falling in the range of modern abyssal peridotites. By contrast, temperatures up to 1400°C were attested for some of the plagioclase lherzolites

of our data set. These elevated values can be explained as related to pyroxene disequilibrium and reactive melt percolation. Closure temperatures models ($T_{BKN}$ vs. $T_{REE}$) indicate that the lherzolites underwent cooling from asthenospheric temperatures at cooling rates of approximately $4 \times 10^{-3}$°C/yr, similar to the oceanic lower crustal lithosphere re-equilibrated through conduction. Similar values ($\approx 10^{-3}$°C/yr) were obtained through Ca in olivine geospeedometer, indicating that cooling rates did not change significantly at lower temperatures.

Temperatures provided by other chemical geothermometers for the lherzolites are also high, covering the range of abyssal peridotites. As a whole, these features may be tentatively ascribed to post-melting evolution and exhumation along a transform fault, in a marginal basin predating Eocene subduction.

Highly refractory, cpx-free, harzburgites constitute the dominant lithology in the New Caledonia ophiolite. These rock types preserve evidence of a high-T evolution testified by $T_{Ca\text{-}in\text{-}Opx}$. $T_{Ca\text{-}in\text{-}Ol}$ and $T_{Ol\text{-}Sp}$, in turn, give relatively high values, similar to modern abyssal peridotites. Cooling rates computed with Ca in olivine thermometer yield values $\approx 10^{-3}$°C/yr. These observations contrast with previous results obtained on ophiolitic peridotites, which generally display lower equilibrium temperatures and cooling rates compared to modern oceanic peridotites. Remarkably, such thermal evolution is also unexpected in forearc mantle sections, where cooling is thought to take place starting from lower initial temperatures and at slower cooling rates. This apparent contradiction may be reconciled with the development of an ephemeral subduction event during Eocene, followed by forearc exhumation and emplacement of the Peridotite Nappe via obduction.

Similar thermal conditions are also recorded by the mafic-ultramafic sequence. The gabbronorites register high $T_{Pl\text{-}Cpx}$, consistent with their derivation from primitive, $H_2O$-poor magmas, transitional towards tholeiites. Major element-based thermometers bear high and constant equilibrium temperatures for the mafic and ultramafic lithologies. Likewise, temperature profiles across the Massif du Sud sequence point to limited temperature variations with depth, that is, from the lower crust to the forearc mantle peridotite. Likewise, Ca in olivine geospeedometer indicate similar cooling rates with depth, in the order of $\approx 10^{-4}$–$10^{-3}$°C/y.

These results are consistent with ascent and injection of non-cogenetic magma batches in a young forearc lithosphere during the early stages of the Eocene subduction, followed by cooling and equilibration at lower T due to obduction.

Our study illustrates how geothermometric investigation of supra-subduction zone ophiolitic complexes can provide crucial insights to unravel the thermal evolution and cooling history of the lithosphere in nascent arc settings. In particular, our results show for the first time that the thermal conditions preserved by forearc lithosphere are only partly inherited from the tectonic setting. Temperature profiles also appear intimately linked to specific geological processes of the investigated area, as well as to the previous lithosphere evolution. Detailed sampling of the different forearc layers and thorough knowledge of the studied area (geology, tectonics etc…) are hence pivotal to unravel the thermal history of such sequences.

We hope that our work motivates further investigation of the New Caledonia ophiolite, possibly combining geothermometric data and geodynamic modeling, to gain new insights into the post-melting evolution, emplacement and obduction of the Peridotite Nappe.

## Data Availability Statement

The data used in this study are included as Tables in the Tables S1, S2, S3 and S4. They are also available in a public data repository at (https://doi.org/10.5281/zenodo.5676145).

**Acknowledgments**
This study has been supported by Italian-PRIN 2017-KY5ZX8. This work has also benefited from the equipment and framework of the COMP-HUB Initiative, funded by the "Departments of Excellence" program of the Italian Ministry for Education, University and Research (MIUR, 2018–2022). In particular, we wish to thank Andrea Comelli for thin section preparation and Luca Barchi for support during SEM-EDS analyses. We also thank J. Blichert-Toft for editorial handling. Constructive reviews by Nick Dygert, Alessio Sanfilippo, John Shervais, and an anonymous reviewer are greatly acknowledged.

## References

Aitchison, J. C., Clarke, L., Meffre, S., & Cluzel, D. (1995). Eocene arc-continent collision in New Caledonia and implications for regional Southwest Pacific tectonic evolution. *Geology*, *23*(2), 161–164. https://doi.org/10.1130/0091-7613(1995)023<0161:eaccin>2.3.co;2

Aldanmaz, E. (2012). Trace element geochemistry of primary mantle minerals in spinel-peridotites from polygenetic MOR-SSZ suites of SW Turkey: Constraints from an LA-ICP-MS study and implications for mantle metasomatism. *Geological Journal*, *47*(1), 59–76. https://doi.org/10.1002/gj.13361336

Avias, J. (1967). Overthrust structure of the main ultrabasic new Caledonian massives. *Tectonophysics*, *4*(4–6), 531–541. https://doi.org/10.1016/0040-1951(67)90017-0

Barth, M. G., Mason, P. R., Davies, G. R., Dijkstra, A. H., & Drury, M. R. (2003). Geochemistry of the Othris Ophiolite, Greece: Evidence for refertilization? *Journal of Petrology*, *44*(10), 1759–1785. https://doi.org/10.1093/petrology/egg058

Basch, V., Borghini, G., Fumagalli, P., Rampone, E., Ferrando, C., & Gandolfo, A. (2019). Plagioclase-facies thermobarometric evolution of the External Liguride pyroxenite-bearing mantle (Suvero, Italy). *Ofioliti*, *45*(1), 1–11.

Batanova, V. G., Belousov, I. A., Savelieva, G. N., & Sobolev, A. V. (2011). Consequences of channelized and diffuse melt transport in supra-subduction zone mantle: Evidence from the Voykar Ophiolite (Polar Urals). *Journal of Petrology*, *52*(12), 2483–2521. https://doi.org/10.1093/petrology/egr053

Brey, G. P., & Köhler, T. (1990). Geothermobarometry in four-phase lherzolites II. New thermobarometers, and practical assessment of existing thermobarometers. *Journal of Petrology*, *31*(6), 1353–1378. https://doi.org/10.1093/petrology/31.6.1353

Burg, J. P., Bodinier, J. L., Chaudhry, S., Hussain, S., & Dawood, H. (1998). Infra-arc mantle–crust transition and intra-arc mantle diapirs in the Kohistan complex (Pakistani Himalaya): Petro-structural evidence. *Terra Nova*, *10*(2), 74–80. https://doi.org/10.1046/J.1365-3121.1998.00170.X

Canil, D., Grundy, R., & Johnston, S. T. (2019). Thermal history of the Donjek harzburgite massif in ophiolite from Yukon, Canada with implications for the cooling of oceanic mantle lithosphere. *Lithos*, *328–329*, 33–42. https://doi.org/10.1016/j.lithos.2019.01.001

Chakraborty, S. (2010). Diffusion coefficients in olivine, wadsleyite and ringwoodite. *Reviews in Mineralogy and Geochemistry*, *72*(1), 603–639. https://doi.org/10.2138/rmg.2010.72.13

Cherniak, D. J., & Dimanov, A. (2010). Diffusion in pyroxene, mica and amphibole. *Reviews in Mineralogy and Geochemistry*, *72*(1), 641–690. https://doi.org/10.2138/rmg.2010.72.14

Cluzel, D., Aitchison, J. C., & Picard, C. (2001). Tectonic accretion and underplating of mafic terranes in the late Eocene intraoceanic fore-arc of New Caledonia (Southwest Pacific): Geodynamic implications. *Tectonophysics*, *340*(1–2), 23–59. https://doi.org/10.1016/S0040-1951(01)00148-007

Cluzel, D., Aitchison, J. C., Secchiari, A., Montanini, A., & Bosch, D. (2020). New Caledonia Ophiolite, Marginal Rifting to Fore-arc Evolution. *Acta Geologica Sinica*, English Edition, *94*(S1), 9–10. https://doi.org/10.1111/1755-6724.14431

Cluzel, D., Jourdan, F., Meffre, S., Maurizot, P., & Lesimple, S. (2012). The metamorphic sole of New Caledonia ophiolite: 40 Ar/39 Ar, U-Pb, and geochemical evidence for subduction inception at a spreading ridge. *Tectonics*, *31*(3). https://doi.org/10.1029/2011TC003085

Cluzel, D., Maurizot, P., Collot, J., & Sevin, B. (2012). An outline of the Geology of New Caledonia; from Permian–Mesozoic Southeast Gondwanaland active margin to Cenozoic obduction and supergene evolution. *Episodes*, *35*(1), 72–86. https://doi.org/10.18814/epiiugs/2012/v35i1/007

Cluzel, D., Meffre, S., Maurizot, P., & Crawford, A. J. (2006). Earliest Eocene (53 Ma) convergence in the Southwest Pacific; evidence from pre-obduction dikes in the ophiolite of New Caledonia. *Terra Nova*, *18*(6), 395–402. https://doi.org/10.1111/j.1365-3121.2006.00704.x

Cluzel, D., Ulrich, M., Jourdan, F., Meffre, S., Paquette, J. L., Audet, M. A., et al. (2016). Early Eocene clinoenstatite boninite and boninite-series dikes of the ophiolite of New Caledonia; a witness of slab-derived enrichment of the mantle wedge in a nascent volcanic arc. *Lithos*, *260*, 429–442. https://doi.org/10.1016/j.lithos.2016.04.031

Coogan, L. A., Jenkin, G. R. T., & Wilson, R. N. (2002). Constraining the cooling rate of the lower oceanic crust: A new approach applied to the Oman ophiolite. *Earth and Planetary Science Letters*, *199*(1–2), 127–146. https://doi.org/10.1016/S0012-821X(02)00554-XX

De Hoog, J. C. M., Gall, L., & Cornell, D. H. (2010). Trace-element geochemistry of mantle olivine and application to mantle petrogenesis and geothermobarometry. *Chemical Geology*, *270*, 196–215.

Dimanov, A., & Wiedenbeck, M. (2006). (Fe, Mn)-Mg interdiffusion in natural diopside: Effect of $pO_2$. *European Journal of Mineralogy*, *18*(6), 705–718. https://doi.org/10.1127/0935-1221/2006/0018-07050705

Dygert, N., Kelemen, P. B., & Liang, Y. (2017). Spatial variations in cooling rate in the mantle section of the Samail ophiolite in Oman: Implications for formation of lithosphere at mid-ocean ridges. *Earth and Planetary Science Letters*, *465*, 134–144. https://doi.org/10.1016/j.epsl.2017.02

Dygert, N., & Liang, Y. (2015). Temperatures and cooling rates recorded in REE in coexisting pyroxenes in ophiolitic and abyssal peridotites. *Earth and Planetary Science Letters*, *420*, 151–161. https://doi.org/10.1016/j.epsl.2015.02.042

Dygert, N., Liang, Y., & Kelemen, P. B. (2016). Formation of Plagioclase lherzolite and associated dunite–harzburgite–lherzolite sequences by multiple episodes of melt percolation and melt–rock reaction: An example from the Trinity Ophiolite, California, USA. *Journal of Petrology*, *57*(4), 815–838. https://doi.org/10.1093/petrology/egw018

Faak, K., & Gillis, K. M. (2016). Slow cooling of the lowermost oceanic crust at the fast-spreading East Pacific Rise. *Geology*, *44*(2), 115–118. https://doi.org/10.1130/G37353.1

Fabriès, J. (1979). Spinel-olivine geothermometry in peridotites from ultramafic complexes. *Contributions to Mineralogy and Petrology*, *69*(4), 329–336. https://doi.org/10.1007/BF00372258

Falloon, T. J., & Danyushevsky, L. V. (2000). Melting of refractory mantle at 1.5, 2 and 2.5 GPa under anhydrous and $H_2O$-undersaturated conditions: Implications for the Petrogenesis of high-Ca boninites and the influence of subduction components on mantle melting. *Journal of Petrology*, *41*(2), 257–283. https://doi.org/10.1093/petrology/41.2.257

Ferrari, E., Secchiari, A., Montanini, A., & Cluzel, D. (2021). *The Bogota pyroxenites (New Caledonia): New insights on mantle heterogeneity in young subduction systems* (p. 96). Italian geological society. 90° Meeting, "Geology without borders" Abstract Book.

Fumagalli, P., Borghini, G., Rampone, E., & Poli, S. (2017). Experimental calibration of Forsterite–Anorthite–Ca-Tschermak–Enstatite (FACE) geobarometer for mantle peridotites. *Contributions to Mineralogy and Petrology*, *172*(6), 38. https://doi.org/10.1007/s00410-017-1352-2

Ganguly, J., & Tirone, M. (1999). Diffusion closure temperature and age of a mineral with arbitrary extent of diffusion: Theoretical formulation and applications. *Earth and Planetary Science Letters*, *170*(1–2), 131–140. https://doi.org/10.1016/S0012-821X(99)00089-8

Garrido, C. J., Bodinier, J. L., Dhuime, B., Bosch, D., Chanefo, I., Bruguier, O., et al. (2007). Origin of the island arc Moho transition zone via melt-rock reaction and its implications for intracrustal differentiation of island arcs: Evidence from the Jijal complex (Kohistan complex, northern Pakistan). *Geology*, *35*(8), 683–686. https://doi.org/10.1130/G23675A.1

Greene, A. R. (2006). A detailed geochemical study of island arc crust: The Talkeetna arc section, South-central Alaska. *Journal of Petrology*, *47*(6), 1051–1093. https://doi.org/10.1093/petrology/egl002

Guo, P., Xu, W. L., Wang, C. G., & Zhang, Y. L. (2019). Thermal state and structure of lithospheric mantle beneath the Xing'an Massif, northeast China: Constraints from mantle xenoliths entrained by Cenozoic basalts. *Geological Journal*, *54*(6), 3226–3238. https://doi.org/10.1002/gj.3322

Hanghøj, K., Kelemen, P. B., Hassler, D., & Godard, M. (2010). Composition and genesis of depleted mantle Peridotites from theWadi Tayin massif, Oman Ophiolite; major and trace element geochemistry, and Os isotope and PGE systematics. *Journal of Petrology*, *51*, 201–227.

Jean, M. M., Shervais, J. W., Choi, S.-H., & Mukasa, S. B. (2010). Melt extraction and melt refertilization in mantle peridotite of the coast range ophiolite: An LA–ICP–MS study. *Contributions to Mineralogy and Petrology*, *159*(1), 113–136. https://doi.org/10.1007/s00410-009-0419-0

Johnson, K. T. M., Dick, H. J. B., & Shimizu, N. (1990). Melting in the oceanic upper mantle: An ion microprobe study of diopsides in abyssal Peridotites. *Journal of Geophysical Research*, *95*(B3), 2661. https://doi.org/10.1029/JB095iB03p02661

Khedr, M. Z., Arai, S., Python, M., & Tamura, A. (2014). Chemical variations of abyssal peridotites in the central Oman ophiolite: Evidence of oceanic mantle heterogeneity. *Gondwana Research*, *25*(3), 1242–1262. https://doi.org/10.1016/j.gr.2013.05.010

Lagabrielle, Y., Chauvet, A., Ulrich, M., & Guillot, S. (2013). Passive obduction and gravity-driven emplacement of large ophiolitic sheets: The New Caledonia ophiolite (SW Pacific) as a case study? *Bulletin de La Societe Geologique de France*, *184*(6), 545–556. https://doi.org/10.2113/gssgfbull.184.6.545

Lee, C. T. A., & Chin, E. J. (2014). Calculating melting temperatures and pressures of peridotite protoliths: Implications for the origin of cratonic mantle. *Earth and Planetary Science Letters*, *403*, 273–286. https://doi.org/10.1016/j.epsl.2014.06.048

Lee, C. T. A., Harbert, A., & Leeman, W. P. (2007). Extension of lattice strain theory to mineral/mineral rare-earth element partitioning: An approach for assessing disequilibrium and developing internally consistent partition coefficients between olivine, orthopyroxene, clinopyroxene and basaltic melt. *Geochimica et Cosmochimica Acta*, *71*(2), 481–496. https://doi.org/10.1016/j.gca.2006.09

Li, J., Kornprobst, J., Vielzeuf, D., & Fabriès, J. (1995). An improved experimental calibration of the olivine-spinel geothermometer. *Chinese Journal of Geochemistry*, *14*(1), 68–77. https://doi.org/10.1007/BF02840385

Liang, Y., Sun, C., & Yao, L. (2013). A REE-in-two-pyroxene thermometer for mafic and ultramafic rocks. *Geochimica et Cosmochimica Acta*, *102*, 246–260. https://doi.org/10.1016/j.gca.2012.10.035

Lindsley, D. H. (1983). Pyroxene thermometry. *American Mineralogist*, *68*(5–6), 477–493.Retrieved from https://pubs.geoscienceworld.org/msa/ammin/article-abstract/68/5-6/477/104808/pyroxene-thermometry

Marchesi, C., Garrido, C. J., Godard, M., Belley, F., & Ferré, E. (2009). Migration and accumulation of ultra-depleted subduction-related melts in the Massif du Sud ophiolite (New Caledonia). *Chemical Geology*, *266*(3–4), 171–186. https://doi.org/10.1016/j.chemgeo.2009.06.004

Marchesi, C., Jolly, W. T., Lewis, J. F., Garrido, C. J., Proenza, J. A., & Lidiak, E. G. (2011). Petrogenesis of fertile mantle peridotites from the Monte del Estado massif (Southwest Puerto Rico): A preserved section of Proto-caribbean lithospheric mantle? *Geologica Acta*, *9*(3), 289–306. https://doi.org/10.1344/105.000001713

McGoldrick, S., Canil, D., & Zagorevski, A. (2018). Contrasting thermal and melting histories for segments of mantle lithosphere in the Nahlin ophiolite, British Columbia, Canada. *Contributions to Mineralogy and Petrology*, *173*(3), 1–17. https://doi.org/10.1007/s00410-018-1450-9

Müntener, O., Manatschal, G., Desmurs, L., & Pettke, T. (2010). Plagioclase Peridotites in ocean-continent transitions: Refertilized mantle domains generated by melt Stagnation in the shallow mantle lithosphere. *Journal of Petrology*, *51*(1–2), 255–294. https://doi.org/10.1093/petrology/egp087

Nicolas, A. (1989). *Structures of ophiolites and dynamics of oceanic lithosphere. Petrology and structural geology* (Vol. 4). Kluwer Academic Publishers.

Ohara, Y., & Ishii, T. (1998). Peridotites from the southern Mariana forearc: Heterogeneous fluid supply in mantle wedge. *Island Arc*, *7*(3), 541–558. https://doi.org/10.1111/j.1440-1738.1998.00209.x

Parkinson, I. J., & Pearce, J. A. (1998). Peridotites from the Izu-Bonin-Mariana forearc (ODP leg 125): Evidence for mantle melting and melt-mantle interaction in a supra-subduction zone setting. *Journal of Petrology*, *39*(9), 1577–1618. https://doi.org/10.1093/petroj/39.9.1577

Pirard, C., Hermann, J., & O'Neill, H. S. C. (2013). Petrology and geochemistry of the crust-mantle boundary in a nascent arc, massif du Sud Ophiolite, New Caledonia, SW Pacific. *Journal of Petrology*, *54*(9), 1759–1792. https://doi.org/10.1093/petrology/egt030

Prinzhofer, A., & Allègre, C. J. (1985). Residual peridotites and the mechanisms of partial melting. *Earth and Planetary Science Letters*, *74*(2–3), 251–265.

Prinzhofer, A., & Nicolas, A. (1980). The Bogota Peninsula, New Caledonia: A possible oceanic transform fault. *The Journal of Geology*, *88* (4), 387–398. https://doi.org/10.1086/628523

Putirka, K. D. (2008). Thermometers and barometers for volcanic systems. *Reviews in Mineralogy and Geochemistry*, *69*(1), 61–120. https://doi.org/10.2138/rmg.2008.69.3

Riches, A. J. V., & Rogers, N. W. (2011). Mineralogical and geochemical constraints on the shallow origin, ancient veining, and multi-stage modification of the Lherz peridotite. *Geochimica et Cosmochimica Acta*, *75*(20), 6160–6182. https://doi.org/10.1016/j.gca.2011.07.036

Schellart, W. P., Lister, G. S., & Toy, V. G. (2006). A Late Cretaceous and Cenozoic reconstruction of the Southwest Pacific region: Tectonics controlled by subduction and slab rollback processes. *Earth-Science Reviews*, *76*(3–4), 191–233. https://doi.org/10.1016/j.earscirev.2006.01.002

Secchiari, A., Montanini, A., Bosch, D., Macera, P., & Cluzel, D. (2016). Lithos Melt extraction and enrichment processes in the New Caledonia lherzolites: Evidence from geochemical and Sr–Nd isotope data. *Lithos*, *260*, 28–43. https://doi.org/10.1016/j.lithos.2016.04

Secchiari, A., Montanini, A., Bosch, D., Macera, P., & Cluzel, D. (2018). The contrasting geochemical message from the New Caledonia gabbronorites: Insights on depletion and contamination processes of the sub-arc mantle in a nascent arc setting. *Contributions to Mineralogy and Petrology*, *173*(8), 66. https://doi.org/10.1007/s00410-018-1496-8

Secchiari, A., Montanini, A., Bosch, D., Macera, P., & Cluzel, D. (2019). Origin of the spinel-pyroxene symplectites in the harzburgites from the New Caledonia peridotite. *Ofioliti*, *44*(1), 31–42. https://doi.org/10.4454/ofioliti.v44i1.463

Secchiari, A., Montanini, A., Bosch, D., Macera, P., & Cluzel, D. (2020). Sr, Nd, Pb and trace element systematics of the New Caledonia harzburgites: Tracking source depletion and contamination processes in a SSZ setting. *Geoscience Frontiers*, *11*(1), 37–55. https://doi.org/10.1016/j.gsf.2019.04.004

Smye, A., Seaman, S., Hudak, M., & Crispin, K. (2017). Rates of mantle cooling and exhumation during rifting constrained by REE-in-pyroxene speedometry. *Geochemistry, Geophysics, Geosystems*, *18*, 1580–1593. https://doi.org/10.1002/2017GC006821

Sun, C., & Liang, Y. (2014). An assessment of subsolidus re-equilibration on REE distribution among mantle minerals olivine, orthopyroxene, clinopyroxene, and garnet in peridotites. *Chemical Geology*, *372*, 80–91. https://doi.org/10.1016/J.CHEMGEO.2014.02.014

Sun, C., & Liang, Y. (2017). A REE-in-plagioclase–clinopyroxene thermometer for crustal rocks. *Contributions to Mineralogy and Petrology*, *172*(4), 1–20. https://doi.org/10.1007/s00410-016-1326-9

Takazawa, E., Okayasu, T., & Satoh, K. (2003). Geochemistry and origin of the basal lherzolites from the northern Oman ophiolite (northern Fizh block). *Geochemistry, Geophysics, Geosystems*, *4*(2) https://doi.org/10.1029/2001gc000232

Taylor, W. R. (1998). An experimental test of some geothermometer andgeobaro-meter formulations for upper mantle peridotites with application to the ther-mobarometry of fertile lherzolite and garnetwebsterite. *Neues Jahrbuch Für Mineralogie - Abhandlungen*, 381–408. https://doi.org/10.1127/NJMA/172/1998/381

Titus, S. J., Maes, S. M., Benford, B., Ferré, E. C., & Tikoff, B. (2011). Fabric development in the mantle section of a paleotransform fault and its effect on ophiolite obduction, New Caledonia. *Lithosphere*, *3*(3), 221–244. https://doi.org/10.1130/L122.1

Ulrich, M., Picard, C., Guillot, S., Chauvel, C., Cluzel, D., & Meffre, S. (2010). Multiple melting stages and refertilization as indicators for ridge to subduction formation: The New Caledonia ophiolite. *Lithos*, *115*(1–4), 223–236. https://doi.org/10.1016/j.lithos.2009.12.011

VanTongeren, J. A., Kelemen, P. B., & Hanghøj, K. (2008). Cooling rates in the lower crust of the Oman ophiolite: Ca in olivine, revisited. *Earth and Planetary Science Letters*, *267*(1–2), 69–82. https://doi.org/10.1016/j.epsl.2007.11.034

Warren, J. M. (2016). Global variations in abyssal peridotite compositions. In *Lithos*. Elsevier. https://doi.org/10.1016/j.lithos.2015.12.023

Warren, J. M., Shimizu, N., Sakaguchi, C., Dick, H. J. B., & Nakamura, E. (2009). An assessment of upper mantle heterogeneity based on abyssal peridotite isotopic compositions. *Journal of Geophysical Research*, *114*(B12), B12203. https://doi.org/10.1029/2008JB006186

Wells, P. R. A. (1977). Pyroxene thermometry in simple and complex systems. *Contributions to Mineralogy and Petrology*, *62*(2), 129–139. https://doi.org/10.1007/BF00372872

Whattam, S. A. (2009). Arc-continent collisional orogenesis in the SW Pacific and the nature, source and correlation of emplaced ophiolitic nappe components. *Lithos*, *113*(1–2), 88–114. https://doi.org/10.1016/j.lithos.2008.11.009

Xu, Y., Liu, C. Z., & Lin, W. (2020). Melt extraction and reaction in the forearc mantle: Constraints from trace elements and isotope geochemistry of ultra-refractory peridotites of the New Caledonia Peridotite Nappe. *Lithos*, *380–381*, 105882. https://doi.org/10.1016/j.lithos.2020.105882

Zanetti, A., D'Antonio, M., Spadea, P., Raffone, N., Vannucci, R., & Brugier, O. (2006). Petrogenesis of mantle peridotites from the Izu-Bonin-Mariana (IBM) forearc. *Ofioliti*, *31*(2), 189–206.